International Journal of Heat and Mass Transfer 183 (2022) 122237

Contents lists available at ScienceDirect

International Journal of Heat and Mass Transfer

journal homepage: www.elsevier.com/locate/hmt

Experimental and computational investigation of flow boiling in microgravity

Jeongmin Lee[a], Issam Mudawar[a,1,*], Mohammad M. Hasan[b], Henry K. Nahra[b], Jeffrey R. Mackey[c]

[a] Purdue University Boiling and Two-Phase Flow Laboratory (PU-BTPFL), School of Mechanical Engineering, Purdue University, 585 Purdue Mall, West Lafayette, IN 47907, USA
[b] NASA Glenn Research Center, 21000 Brookpark Road, Cleveland, OH 44135, USA
[c] HX5, LLC, 3000 Aerospace Parkway, Brook Park, OH 44142, USA

ARTICLE INFO

Article history:
Received 12 May 2021
Revised 22 October 2021
Accepted 7 November 2021
Available online 28 November 2021

Keywords:
Two-phase cooling
Flow boiling
CFD
Microgravity

ABSTRACT

This study explores use of Computational Fluid Dynamics (CFD) to predict near-saturated flow boiling of FC-72 in microgravity. The computational method employs transient analysis to predict detailed interfacial behavior and heat transfer characteristics along a rectangular channel heated along two opposite walls. Predicted results are validated against experimental temperature measurements and high-speed video images captured during a series of parabolic aircraft maneuvers for three sets of operating conditions which include variations of both mass velocity and wall heat flux. The computational method is based on the multi-phase volume of fluid (VOF) model, which is combined with appropriate phase change and turbulence models, and accounts for both shear-lift force on bubbles and conjugate heat transfer along the heating walls. A key advantage of the CFD method is ability to capture details that are very difficult to measure experimentally, including detailed spatial variations of bubble shape, void fraction, mixture fluid temperature, liquid velocity, and vapor velocity, results for which are presented for each of the three test cases. Different flow regimes predicted along the heated length exhibit a number of dominant mechanisms including bubble nucleation, bubble growth, coalescence, vapor blankets, interfacial waviness, and residual liquid sub-layer, all of which agree well with experiment. Vapor velocity is shown to increase appreciably along the heated length because of increased void fraction, while liquid velocity experiences large fluctuations. Non-equilibrium effects are accentuated with increasing mass velocity, contributing minor deviations of fluid temperature from simulations compared to those predicted by the analytical method. Predicted wall temperature is fairly uniform in the middle of the heated length but increases in the entrance region, due to sensible heat transfer in the subcooled liquid, and decreases toward the exit, mostly because of flow acceleration resulting from increased void fraction.

1. Introduction

1.1. Importance of two-phase cooling to space missions

The recent intensified interest in space missions to the Moon, Mars and beyond has spurred space agencies worldwide to aggressively pursue new system architectures aimed at greatly enhancing mission capability. Examples include not only the missions to the Moon and Mars, but also Lunar and Martian habitat and missions to deep space.

Future manned space missions are expected to increase in distance, duration and therefore power requirements. Enhancing mission performance is contingent on ability to enhance energy efficiency and reduce both size and mass for all subsystems in a space vehicle. Examples include nuclear power generation for deep space missions, cryogenic storage and transfer, and vehicle thermal management. The latter is tackled using a Thermal Control System (TCS), which is responsible for maintaining temperature and humidity inside the space vehicle (also planetary habitat). During the past two decades, NASA reports have pointed to the enormous potential of two-phase thermal management to greatly reduce size and mass of TCS components compared to a TCS utilizing single-phase liquid [1]. A key drawback of the single-phase liquid TCS is reliance on sensible heat alone to both acquire and transport the

* Corresponding author.
E-mail address: mudawar@ecn.purdue.edu (I. Mudawar).
[1] https://engineering.purdue.edu/BTPFL

https://doi.org/10.1016/j.ijheatmasstransfer.2021.122237
0017-9310/

Nomenclature

c_p	specific heat at constant pressure (J/kg·K)
Δc	computational cell height normal to the surface (mm)
E	energy per unit mass (J/kg)
F	force (N/m^3)
G	mass velocity (kg/m^{2}s)
g	gravitational acceleration (m/s^2)
H	longer dimension of flow channel's cross section (mm)
h	enthalpy (J/kg)
h_{fg}	latent heat of vaporization (J/kg)
I	turbulence intensity
k	thermal conductivity (W/m·K)
k_{eff}	effective thermal conductivity (W/m·K)
L_d	development length of flow channel in experiment (mm)
L_e	exit length of flow channel in experiment (mm)
$L_{entrance}$	entrance length in computational domain (mm)
L_{exit}	exit length in computational domain (mm)
L_h	heated length of flow channel (mm)
$\dot{m}$	volumetric mass transfer (kg/m^{3}s)
n_w	direction normal to the wall
P	pressure (Pa)
Pr	Prandtl number
q''	heat flux (W/m^2)
$\bar{q}''$	spatially averaged surface heat flux (W/m^2)
Re	Reynolds number
r_i	mass transfer intensity factor (1/s)
S_h	volumetric energy source (W/m^3)
T	temperature (°C, K)
T^*	dimensionless temperature
$\bar{T}$	spatially averaged temperature (°C, K)
t	time (s)
t_s	thickness of wall in computational domain (mm)
t_w	direction tangential to the wall
u	velocity (m/s)
u_c	compression velocity (m/s)
W	heated width of flow channel (mm)
x	x-direction coordinate
x_e	thermodynamic equilibrium quality
y	y-direction coordinate
z	z-direction coordinate (flow direction)

Greek symbols

α	volume fraction; void fraction
$\bar{\alpha}$	spatially averaged volume fraction of vapor evaluated on surface
Γ	mass transfer rate (kg/m^{3}s)
ε	turbulent dissipation rate (m^2/s^3)
θ_w	contact angle (°)
μ	dynamic viscosity (kg/m·s)
ρ	density (kg/m^3)

Subscripts

D	hydraulic diameter
e	Earth (terrestrial condition)
f	liquid
g	vapor
in	inlet
m	mixture
sat	saturation
sub	subcooling
w	wall

heat. A two-phase TCS, on the other hand, capitalizes on both sensible and latent heat to acquire the heat from cabin and avionics, and reject it via a condenser/radiator to deep space. The size and mass reductions with a two-phase TCS are attributed to orders of magnitude enhancement in heat transfer coefficients associated with both flow boiling and condensation. However, implementation of flow boiling and condensation will require a thorough understanding of how these heat transfer modes are influenced by reduced gravity [2]. The present study concerns the influence of reduced gravity on flow boiling.

1.2. Implementation of boiling in microgravity

The merits of boiling heat transfer in microgravity have been explored for nearly six decades. While capillary-based TCS (conventional heat pipes, loop heat pipes and capillary pumped loops) are still widely used in space systems (especially satellites), these systems are quite limited in terms of both heat flux and total heat load capabilities [3]. This explains the intense interest in pool boiling in microgravity dating back to the early 1960s and continuing into the first decade of the 21st century [4–6].

However, it is presently recognized that pool boiling poses severe challenges when implemented in microgravity, key among which is that bubbles grow to very large size and tend to coalesce with neighboring bubbles with higher frequency (compared to pool boiling in Earth gravity), culminating in the formation of a large 'primary' bubble that covers a significant part of heated surface as well as interrupts the liquid replenishment process. This unique interfacial behavior accelerates dryout on the heated surface, resulting in unusually low values of critical heat flux (CHF).

A more effective strategy to ensuring viability of boiling in microgravity is to utilize a pumped fluid system [7,8]. In the absence of a body force to remove vapor bubbles from the boiling surface, flow boiling can augment cooling performance by relying on bulk liquid motion to flush bubbles away from the heated surface. Here, liquid drag causes bubbles to initially slide along the heated surface, while induced shear serves to the lift the bubbles away from the surface (the lift effect will be described in a later section). These forces resist formation of large insulating vapor masses as well as help maintain the liquid replenishment. Overall, these merits of flow boiling to enhance heat transfer coefficient and CHF can be amplified and effects of reduced body force nullified by increasing the flow velocity.

Since the mid-1980s, investigators at the Purdue University Boiling and Two-Phase Flow Laboratory (PU-BTPFL), including two authors of the present study, have explored implementation of a broad variety of flow boiling schemes, specifically the development of means for CHF enhancement. They include falling film [9], macro- and micro-channel [10–13], jet [14], and spray [15], as well as configurations involving combined use of micro-channels and jets [16].

1.3. Computational fluid dynamics (CFD) modeling of flow boiling in terrestrial and reduced gravity

The vast majority of studies concerning prediction of pressure drop and heat transfer coefficient for flow boiling relies on empirical or semi-empirical formulations. The former is derived entirely from experimental data (e.g., [17–21]) while the latter is based on theoretical (mechanistic) premises but fitted with empirical constants derived from experimental data for closure (e.g., [22–24]). Given their ease of use, both methods are very popular for design of thermal systems. However, their applicability is limited by reliance on data for a few fluids and which are measured over limited ranges of operating conditions. A key limitation of the same methods to design of space subsystems is reliance on experiments

that are performed in Earth gravity, rendering their applicability to microgravity very questionable.

Another class of predictive tools for both flow boiling and flow condensation is theoretical models. Despite their theoretical appeal and relative ease of implementation, these models are often limited to specific flow patterns and/or operating conditions. In fact, most are focused entirely on the annular flow regime, given the simplicity of modeling provided by fully separated liquid and vapor phases (e.g., [25–28]). Additionally, flow boiling in practical devices often involves a succession of different flow patterns along the flow direction, not only annular flow.

The third class of predictive tools is Computational Fluid Dynamics (CFD), which has emerged as a very powerful design tool for a broad range of industries, including electronics, automotive, aerospace, and defense. A key attribute of CFD is ability to predict spatial and temporal flow behavior and heat transfer characteristics, which are difficult to measure experimentally. CFD generally allows simulation of fluid flow without assumptions regarding macroscopic flow patterns. Another important advantage is ability to tackle geometrically complex flows. These merits have led to increased reliance on CFD for analysis of important flow related phenomena as well as analysis and design of flow components or entire system, and eventual optimization of such a system. However, while these merits are easily realized with single-phase flows, they are far less so for multiphase flows, especially where the phases are dispersed together. Another source of complexity is modeling of turbulence effects. Unlike single phase flows, multiphase flows pose the challenges of modeling complex details of flow structure, such as bubble shape and its impact on interphase mass, momentum and energy transport, effects of deformation rate on bubble coalescence and breakup, and formation of macroscopic structures. Modeling turbulent effects pose yet additional difficulties.

Direct numerical simulation (DNS) represents a specific branch of CFD in which the Navier-Stokes equations are numerically solved and entire range of spatial and temporal scales of turbulence resolved instead of relying on Reynolds-averaged Navier-Stokes equations. A good example of a two-phase configuration successfully modeled using DNS is bubble growth and heat transfer associated with slug flow [29]. DNS was also coupled with a level-set (LS) method [30] to track interface between phases and predict flow boiling heat transfer in a finned microchannel. However, given unusually high computational demands, DNS has been successful in modeling mostly small computational domains.

Recent advances in both multiphase flow modeling and computing performance have led to development of new, robust CFD methods. Capture of hydrodynamic interactions between phases is key to accurate simulation of flow boiling processes. Currently, two approaches are widely used: Lagrangian and Eulerian. The former uses moving meshes to track interfacial behavior with a high degree of accuracy. However, repeated remeshing requires enormous computing time, which limits this method to rather simple two-phase problems, such as evolution of single bubble shape and size during flow boiling. On the other hand, the Eulerian method tracks liquid and vapor motion using a fixed grid, which significantly reduces computational expense while offering relatively good predictive accuracy. This explains the wide adoption of this method in numerous commercial CFD packages. The Eulerian approach is typically coupled with the LS method or Volume-of-Fluid (VOF) method [31] to track liquid-vapor interfaces.

Most published flow boiling CFD works have focused on terrestrial gravity conditions [32–36]. Recently, however, a few research groups extended use of CFD to operation ranging from hyper gravity to microgravity. For example, Darzi and Park [37] examined hydrodynamic characteristics of horizontal vapor-liquid plug and bubbly flows of two pairs of fluids, air-water and air-oil, under gravity levels from 10^{-4} to $2g_e$. Using VOF and SST k-ω models, they were able to predict buoyancy effects on flow patterns in absence of phase change quite well. In another study, Bahreini et al. [38], used CFD to simulate flow pattern changes during flow boiling of HFE-7100 along a mini-channel under both terrestrial and reduced gravity. Their simulations, which employed Color-Function VOF (CF-VOF), showed good agreement with experimental data. Agarwal and Dondapati [39] used the Eulerian method to investigate hydrodynamic characteristics and morphology of liquid hydrogen flow boiling under both terrestrial gravity and microgravity. Zheng et al. [40] used the Euler-Eulerian model along with the wall heat flux partition (WHFP) model to predict wall temperature distribution and CHF location for liquid hydrogen flow boiling under various gravity conditions.

1.4. Objectives of present study

The present study is part of a joint project between PU-BTPFL and NASA Glenn Research Center that was initiated in 2012 to develop the Flow Boiling and Condensation Experiment (FBCE) for eventual deployment on the International Space Station (ISS). The ultimate objectives of FBCE are to acquire flow boiling and condensation databases in microgravity, and to develop relevant mechanistic models as well as minimum flow rate criteria required to ensure gravity-independent flow boiling and condensation heat transfer. This study concerns the flow boiling aspects of FBCE.

The work discussed in this paper is comprised of two parts, experimental and computational. The experimental portion involves flow boiling of FC-72 in microgravity, which is simulated in a series of parabolic flight maneuvers. The experiments are conducted in a rectangular channel fitted with two opposite heating walls, and include variations in inlet mass velocity, inlet subcooling, and wall heat flux. Another important aspect of the experiments is use of high-speed video to explore axial development of interfacial features along the channel.

The computational portion of the study involves simulating select operating conditions from the experiments with the aim of predicting hydrodynamics and heat transfer characteristics. The VOF model is adopted to capture details of the interfacial behavior, including nucleation, bubble departure, vapor accumulation in the near-wall region, coalescence, and bubble breakup. A 3D computational domain is adopted which captures precise size and shape of the heated portion of the experimental channel, and with identical inlet and wall heating conditions, also accounting for conjugated heat transfer. The 3D model also provides careful assessment of interfacial phase change and surface tension force. A key feature of the computational methodology is modeling of shear-lift force, which is implemented as a User-Defined Function (UDF) to improve prediction of vapor bubble detachment. The computational work is a follow-up to previous work by two of the present authors involving 2D [41] and 3D [42,43] simulations of flow boiling for vertical upflow in terrestrial gravity. Aside from being focused entirely on microgravity conditions, the present work is intended entirely for near-saturated as opposed to highly subcooled inlet conditions of all three prior studies.

The computational results are validated against experiment for different mass velocities and wall heat fluxes with near-saturated inlet conditions. The computational method is used to investigate and predict vital characteristics of flow boiling which cannot be easily obtained from experiment, including fluid temperature, fluid velocity, void fraction, and turbulent dissipation, both across and along the flow channel.

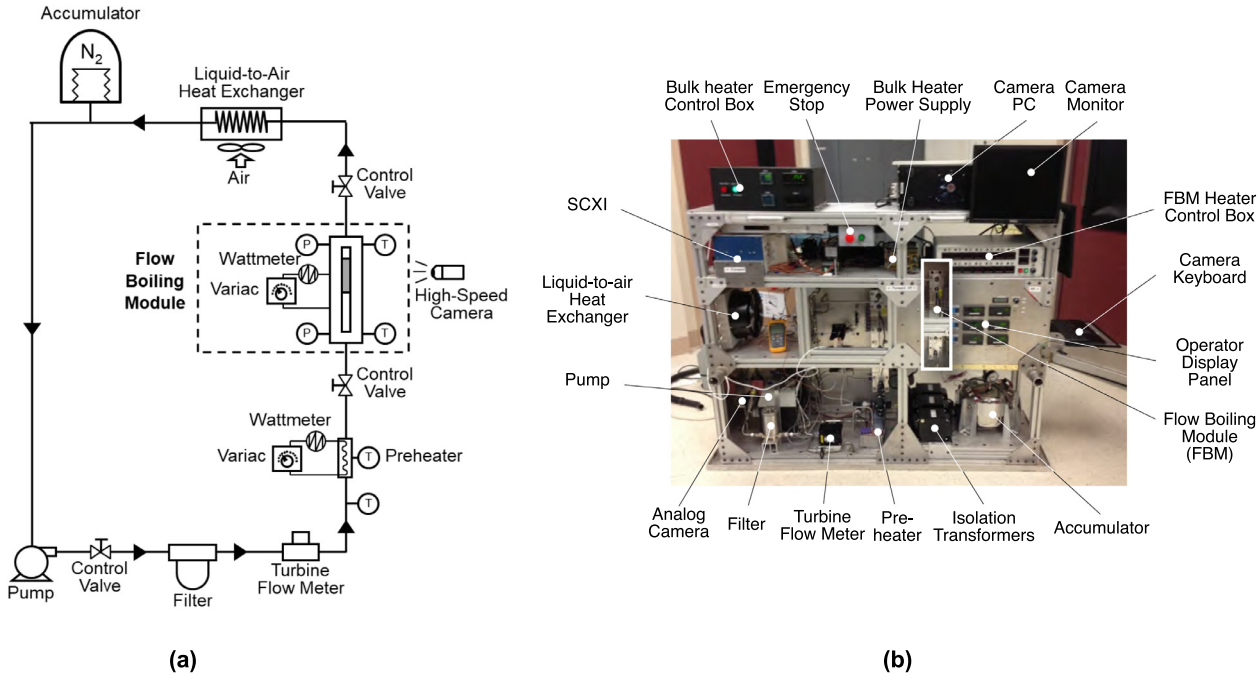

Fig 1. (a) Schematic diagram of flow loop. (b) Photo of parabolic flight facility.

2. Experimental methods

2.1. Flow boiling facility

The test facility used in this study serves to simulate microgravity operation of NASA's Flow Boiling and Condensation Experiment (FBCE), which is due for testing onboard the ISS starting late 2021. Microgravity in the present study is achieved in a series of parabolic maneuvers on a modified Boeing 727 aircraft, with microgravity duration per maneuver of 15–20 s.

Fig. 1(a) shows a schematic of the two-phase flow loop that is used to supply the working fluid, FC-72, to the Flow Boiling Module (FBM) at desired operating conditions; a photo of the entire parabolic flight facility (with key components labeled) is shown in Fig. 1(b). The loop is carefully deaerated prior to a series of tests to rid the FC-72 from any non-condensable gases. During the flight tests, the working fluid is circulated through the closed flow loop with the aid of a magnetically coupled gear pump. Exiting the pump, the liquid is routed through a control valve, a filter, and a turbine flow meter. The liquid then enters a Watlow CAST X-500 circulation heater, where its temperature is raised to desired level, before entering the FBM. All data are obtained in a vertical upflow orientation relative to the aircraft floor. Electric power is supplied to opposite heating walls of FBM causing boiling of the fluid. The mixture exiting the FBM is returned to liquid state after passing through an air-cooled heat exchanger. Located downstream of the condenser is a nitrogen-filled accumulator which is used to set a reference pressure point for the loop.

2.2. Construction of flow boiling module (FBM)

The FBM is designed to enable thermal measurements while simultaneously conducting high-speed video motion analysis of interfacial features. Shown in exploded view in Fig. 2(a), the FBM consists of three transparent polycarbonate plastic plates that are bolted together between two aluminum support plates. The rectangular flow channel is formed by machining a 5.0 mm high by 2.5 mm wide slot into the central axis of the channel's sidewall plate. The inner surfaces forming the front and back walls of the flow boiling channel are polished to optical quality. Both outer channel's top and bottom plastic plates are milled out to insert 15.5 mm wide, 114.6 mm long, and 1.04 mm thick oxygen-free copper slabs that serve as heating walls for the FBM.

Fig. 2(b) depicts an assembled view of the FBM labelled with locations of the fluid's pressure and temperature measurements. Pressure is measured at several locations along the central axis of the flow channel using four pressure taps in the top plastic plate placed equidistantly between the FC-72 inlet port and immediately upstream of the copper heating slabs, with an additional pressure tap placed downstream of the copper slabs. Type-E thermocouples are inserted in the middle of the flow channel through the bottom plastic plate using a metal fitting near the inlet and outlet FC-72 ports.

Shown in Fig. 2(c) is a honeycomb flow straightener affixed upstream at the channel inlet to break any eddies and help straighten the flow. An entry development length 100 times the channel hydraulic diameter provides a hydrodynamically fully developed flow prior to reaching the copper heating slabs. Fig. 2(c) also shows all key dimensions of the channel, including flow development length, L_d = 327.9 mm, heated length, L_h = 114.6 mm, and exit length, L_e = 60.9 mm, in addition to height, H = 5.0 mm, and width, W = 2.5 mm, of the channel's cross-section. The flow is heated along width W with the aid of two thin copper slabs placed opposite to one another, with the central transparent polycarbonate plate providing adiabatic sidewalls for the rectangular flow area.

Wall heating is provided by six 4.5 mm wide by 16.4 mm long 188-Ω thick-film resistors soldered to the backside of each copper slab. Resistors for each slab are connected electrically in parallel and powered by a variable voltage transformer. Two sets of seven Type-E thermocouples are inserted into shallow holes along the centerline of each copper slab between resistors; one set is used for temperature measurements and the other to activate a relay that cuts off power supply should CHF is detected.

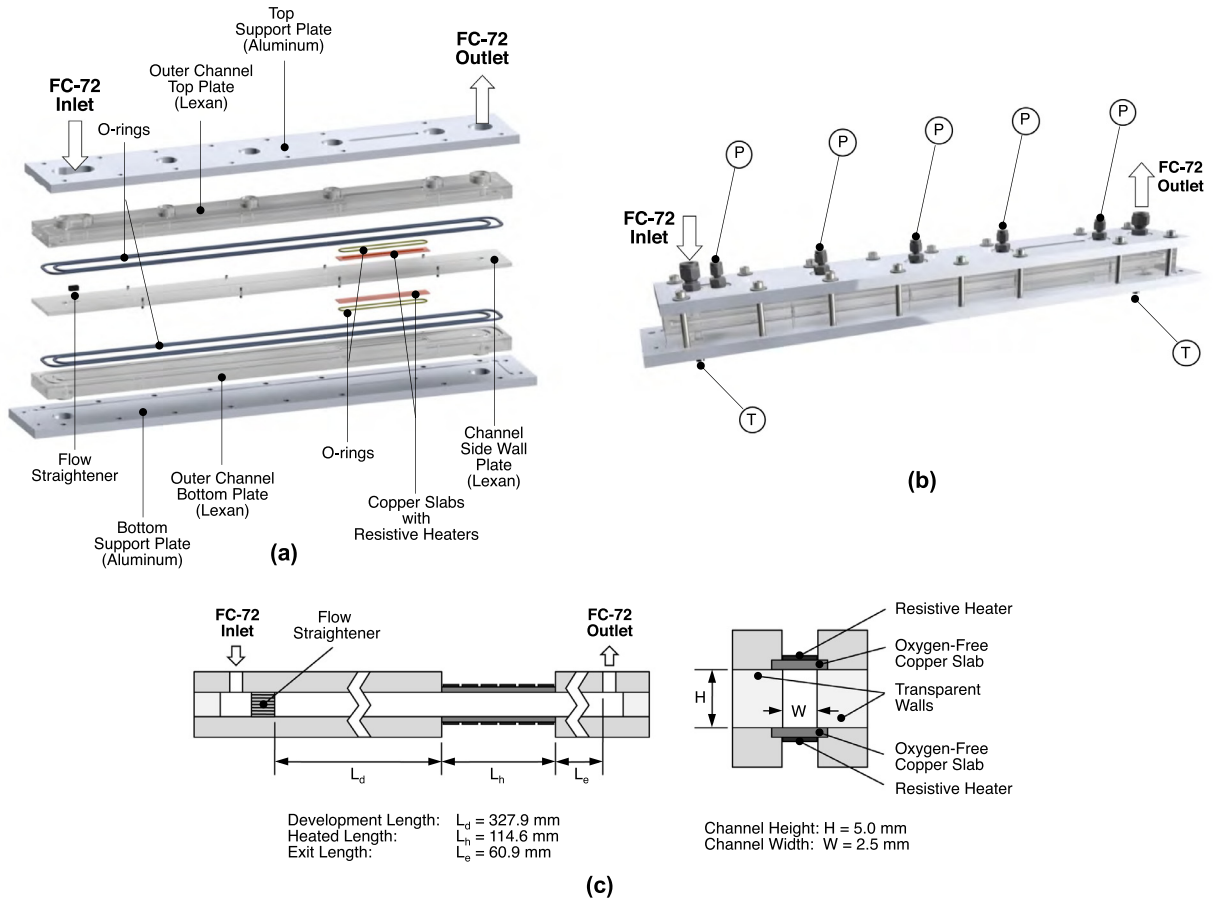

Fig. 2. (a) Exploded view of Flow Boiling Module (FBM). (b) Assembled view of FBM. (c) Key dimensions of flow channel.

2.3. Flow visualization technique

A high-speed camera is used to capture the two-phase interfacial features along the heated portion of the flow channel. A fixed frame rate of 2217 frames per second (fps) and 2040 × 156 pixel resolution (see Fig. 3(a)) facilitate video capture of the entire heated length. Each video image sequence consists of 3000 frames, or 1.353 s of flow visualization data per test run. Illumination is provided from the backside of the flow channel by two LEDs, with a light shaping diffuser (LSD) situated between the LEDs and the channel to enhance illumination uniformity.

Fig. 3(b) shows some image quality is slightly compromised due to (i) barrel distortion caused by the camera lens and (ii) defocus regions near the top and bottom of the boiling image. As shown in Fig. 3(a), the images are obtained starting at pixel element (0,0) and ending at (2040, 156) to produce images 2040 pixels horizontally by 156 pixels vertically.

2.4. Instrumentation and experimental uncertainty

A program is written for use with a data acquisition system to record instrument data throughout the facility. Fluid and wall temperatures are measured with type-E thermocouples having ± 0.5 °C accuracy. Absolute pressure transducers having an accuracy of ± 0.05% are used to measure pressures at several locations along the FBM and the flow loop. The turbine flow meter has an accuracy of ± 0.1%, and accuracy of the FBM heaters is ± 0.5 W and the preheater ± 1 W.

3. Computational methods

3.1. Computational sub-models and key constituent formulations

Microgravity channel flow boiling is simulated with transient analysis in ANSYS-Fluent and a 3D computational domain to track interfacial behavior between liquid and vapor. The computational method employs the VOF approach for multi-phase tracking and the shear stress transport (SST) k-ω turbulence model with turbulence damping and viscous heating to account for eddy dissipation effects within the flow channel. In two-phase bubbly flow, shear stress is influenced by velocity fluctuations inherent to the turbulence liquid flow as well as additional turbulence induced by bubble agitation [44,45]. Turbulence in the liquid phase also plays a crucial role in determining void fraction distribution both across and along the channel [46,47]. According to early works [48,49,50], bubble-induced turbulent mixing enhances convective heat transfer during flow boiling, and turbulence damping and eddy dissipation at the interface are important to accurate calculation of temperature gradient across the interface. Therefore, use of an appropriate turbulence model is essential to accurate prediction of fluid flow and heat transfer characteristics in flow boiling. Prior work [50] has shown that the SST k-ω model provides superior predictions of temperature gradients near the liquid-vapor interface by accounting for turbulence damping. This turbulence model also accounts of low Reynolds number effects and shear stress spreading. Explicit scheme for volume fraction spatial discretization is used to track details of interfacial features every time step with the aid of Geo-Reconstruction method (piecewise-linear approach), thereby ensuring attainment of sharp interface morphol-

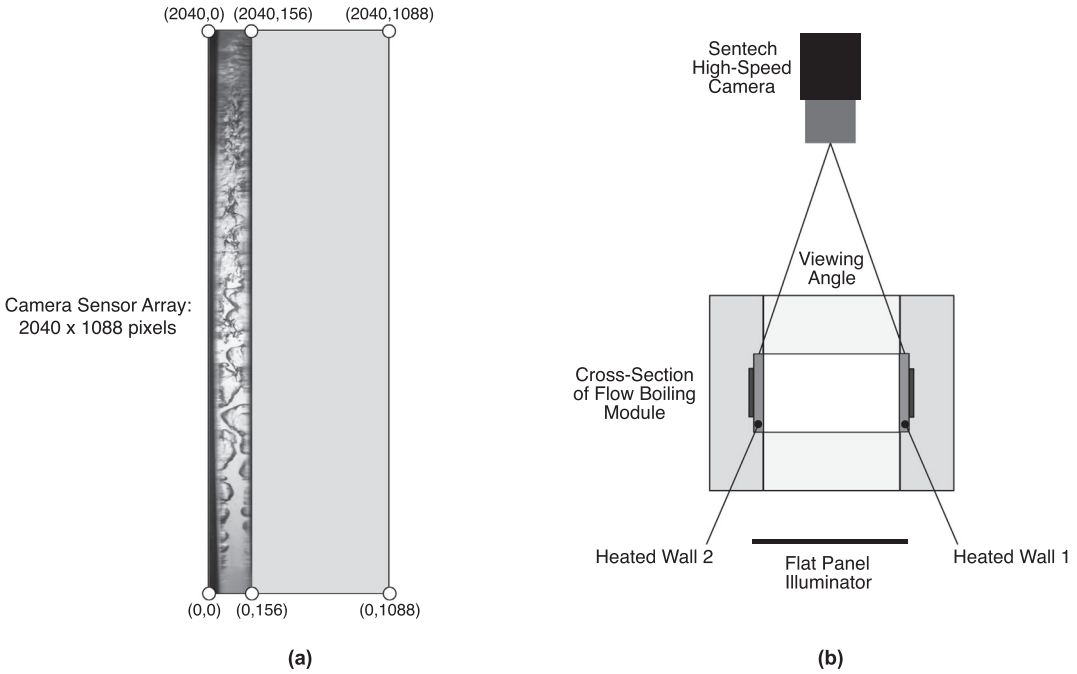

Fig. 3. (a) Resolution of high-speed video camera image encompassing entire heated region of flow channel. (b) Viewing angle of camera and back lighting.

ogy. Because of limitations of the Finite Volume Method (FVM), poor mesh resolution can cause the interface to spread over multiple layers of cells, reducing the accuracy of the computational results [51,52]. Excess numerical diffusion at interfacial cells, which can arise from fluid advection and high aspect-ratio cells, is suppressed by anti-diffusion treatment, which adds a negative diffusion source term, $-\nabla\cdot(\vec{u}_c\alpha(1-\alpha))$, in the volume fraction equation [53,54].

To simplify the two-phase problem in pursuit of better computational tractability, several assumptions are made, key among them are:

(1) The vapor and liquid phases are incompressible and immiscible.
(2) For each set of operating conditions, constant vapor and liquid physical properties are assumed, which is justified by very minor pressure drop measured in experiments.

Volume of fraction of liquid and vapor phases is computed for the entire computational domain (except solid wall) by solving the following respective continuity equations using the VOF formulation:

$$\frac{1}{\rho_g}\left[\frac{\partial}{\partial t}(\alpha_g\rho_g)+\nabla\cdot(\alpha_g\rho_g\vec{u}_g)=S_{\alpha_g}+\sum\left(\dot{m}_{fg}-\dot{m}_{gf}\right)\right], \quad (1)$$

where α, $\vec{u}$, $\dot{m}$, and ρ are volume fraction, velocity, mass transfer rate, and density, respectively, with subscripts f and g referring to liquid and vapor phases. The volume fraction equation is not solved for the liquid phase but computed based on the constraint that the sum of volume fractions in each cell is always equal to unity.

The momentum and energy conservation equations are solved for the entire computational domain in which physical properties in a cell are expressed as volume fraction averages of properties of the individual phases. The momentum and energy conservation equations are expressed, respectively as

$$\frac{\partial}{\partial t}(\rho\vec{u})+\nabla\cdot(\rho\vec{u}\vec{u})=-\nabla P+\nabla\cdot\left[\mu\left(\nabla\vec{u}+\nabla\vec{u}^T\right)\right]+\rho\vec{g}+\vec{F}, \quad (2)$$

and

$$\frac{\partial}{\partial t}(\rho E)+\nabla\cdot(\vec{u}(\rho E+P))=\nabla\cdot\left(k_{eff}\nabla T\right)+S_h, \quad (3)$$

where P, E, $\vec{F}$, and S_h refer to pressure, specific internal energy per unit volume, force vector, and source term per unit volume. Surface tension force is computed using the Continuum Surface Force (CSF) model [55]. For wall adhesion, the liquid-vapor interface normal to a cell near the wall is computed by specifying contact angle, which is given by

$$\hat{n}=\hat{n}_w\cos\theta_w+\hat{t}_w\sin\theta_w, \quad (4)$$

where $\hat{n}_w$ and $\hat{t}_w$ are, respectively, normal and tangential unit vectors relative to the wall, and θ_w is the contact angle. The latent heat by phase change in the energy equation is the product of mass transfer rate and enthalpy difference between liquid and vapor.

The shear-lift force formulation proposed by Klausner et al. [56] and validated over a wide range of Reynold numbers is employed in the present work using a user-defined function (UDF). Due to limitations of the current multiphase model, relative velocity between liquid flow and a vapor bubble attached to the heated surface cannot be accurately computed, resulting in underprediction of bubble departure. This force can have a strong influence on bubble detachment in a liquid boundary layer, and serves to drive bubbles motion away from, and bulk liquid toward, the wall. Accounting for this force is therefore paramount to accurate modeling of flow boiling heat transfer behavior. Extensive details of the numerical model and algorithm used to account for the shear-lift force are provided in prior work by two of the present authors [42].

Phase change simulations require accurate modeling of mass transfer across liquid-vapor interfaces. In recent works, the Lee model [57] has been especially popular for such calculations because of its effectiveness at predicting evaporation in bulk flow at any location where fluid temperature exceeds local saturation temperature. According to this model, the mass transfer rates per unit

volume are expressed as

$$\dot{m}_{fg} = r_i \alpha_f \rho_f \frac{\left(T_f - T_{sat}\right)}{T_{sat}} \quad \text{for evaporation,} \tag{5}$$

and

$$\dot{m}_{gf} = r_i \alpha_g \rho_g \frac{\left(T_{sat} - T_g\right)}{T_{sat}} \quad \text{for condensation.} \tag{6}$$

According to these equations, a local cell filled with superheated liquid will experience evaporation while nothing will happen if it is subcooled. On the other hand, a cell filled with vapor will incur condensation for subcooled conditions. modeling of nucleation site density and locations is not required, and a random distribution of vapor bubble nucleation sites along the heated walls is created initially by numerical truncation error [38]. Notice that the amount of evaporation or condensation is highly dependent on the magnitude of mass intensity factor, r_i (having units of s^{-1}), which is not universal to different phase change environments. Therefore, the value of r_i adopted in a given simulation must be tuned based on working fluid, flow geometry, computational mesh, and operating conditions. In general, high r_i values can cause unstable numerical convergence and low r_i discrepancies between interface and saturation temperatures. While using identical r_i values for both evaporation and condensation is a common practice, this assumption was shown in [42] to culminate in appreciable discrepancies in vapor bubble formations between simulation and experiment. The same study showed predictions were especially sensitive to the value of r_i for evaporation. After exploring a range of r_i values, best predictions for 3D simulations were achieved using the values $r_i = 100\ s^{-1}$ for evaporation and $0.1\ s^{-1}$ for condensation. One key difference between this earlier study and the present is inlet subcooling, ~34 °C versus near-saturated. However, since fluid in core region of the flow channel in the present study is nearly saturated, interfacial mass transfer is dominated by evaporation and to a far lesser extent by condensation, which justifies using $r_i = 100\ s^{-1}$ for evaporation and $0.1\ s^{-1}$ for condensation over the entire computational domain in the present simulations as well.

3.2. Computational domain and boundary conditions

The present study simulates near-saturated flow boiling of FC-72 along a rectangular channel having a 2.5 × 5 mm ($W \times H$) cross section, where heat is supplied to the two opposite shorter walls and the longer walls are adiabatic. As shown in Fig. 4(a), the length of the 3D computational domain consists of three regions: upstream unheated length of $L_{entrance} = 5$ mm (small length used here is based on the fact that the flow in experiment is fully developed upstream of the heated length), heated length of $L_h = 114.6$ mm, and downstream unheated length of $L_{exit} = 10$ mm. Incorporating the entrance and exit lengths is intended to eliminate any potential numerically induced entrance/exit effects. The 3D domain is constructed using ANSYS ICEM including details vital to determining heat transfer boundary conditions and accounting for conjugate heat transfer effects. This includes full thicknesses of the two 1.04 mm thick copper slaps and actual locations of heating surfaces of the six resistive heaters soldered to the backside of each copper slab. Notice in Fig. 4(a) that, while the parabolic flight experiments are intended to simulate microgravity conditions, a very small residual gravity ($g \sim 0.05\ m/s^2$, opposite to the flow direction) is measured on the aircraft and accounted for.

As shown in Fig. 4(b), the computational mesh consists of ~1,970,000 quadrilateral cells and ~1,850,000 nodes, which was confirmed for solution convergence. A uniform mesh with grid size Δc of ~0.120 mm is adopted for the core region, while near-wall mesh is refined to $\Delta c = 0.006$ mm to better capture large velocity, shear, and temperature gradients, which is vitally important to accurate prediction of bubble growth and trajectory. As discussed in [42], the near-wall cell size of $\Delta c = 0.006$ mm ensures that non-dimensional distance, y^+, from the heated wall is below 5 along the entire channel length, thereby ensuring ability to capture flow details within the viscous sublayer. Note that, while micro-scale evaporation effects along the contact line have been successfully used in small domain situation (e.g., pool boiling) [58], coupling micro-scale effects and conventional CFD simulations for flow boiling in a large domain is generally avoided in most recent flow boiling investigations because of prohibitively long computing time and associated resources and cost.

The simulations are conducted using dielectric coolant FC-72 as working fluid for three representative experimental test cases with fairly constant inlet pressure (P_{in} = 120.3 – 133.4 kPa) and near-saturated inlet conditions ($\Delta T_{sub,in}$ = 5.14 to 6.23 °C, $x_{e,in}$ = −0.07 to −0.09). The primary parameters used, which are identical to those from experiment, are mass velocity, G = 200.5, 444.1, and 758.9 kg/m^{2}s, and heat flux, q'' = 75, 176, and 193 kW/m^2. The heat flux values correspond only to heating surfaces of the six thick film resistors indicated in Fig. 4(a), and the 75, 176 and 193 kW/m^2 correspond to 37, 69 and 67% of the measured CHF based on total wetted area of copper slab. Complete details for all three cases are provided in Table 1.

A coupled heat transfer boundary is applied to the interface between solid and fluid cells to properly address conjugate heat transfer effects. Because the flow channel in experiment features a very long entrance region, the flow entering the computational domain is assumed to acquire fully developed velocity profile, with turbulent intensity calculated according to empirical correlation [59], $I = u'/\bar{u} = 0.16\mathrm{Re}_D^{-1/8}$. A uniform outlet pressure equal to that measured from the corresponding parabolic flight experiment is applied to the exit. Non-slip boundary conditions are applied to all channel walls, and a contact angle of $\theta_w = 175°$ (defined from the inside of a vapor bubble to the liquid-vapor interface at the wall) in the surface tension model to account for wall adhesion effects. It is important to note the difficulty in defining a dynamic contact angle along with the contact line of a vapor bubble with diverse shape in a 3-D computational domain. It is for this reason that the surface tension effects in the present study are tackled using static contact angle. While the parabolic flight experiments are intended to simulate microgravity conditions, a very small residual gravity of $g = 0.05\ m/s^2$ measured on the aircraft is employed, which points to minimal buoyancy forces exerted on vapor bubbles. Variable time-step size from 10^{-5} to 10^{-7} s and a global Courant number ($u\Delta t/\Delta c$) of unity are used to ensure numerical stability. This study employed 72 cores of Xeon Gold “Sky Lake” processors per case which yielded convergence in about two months. Table 2 provides values of the physical properties used in the simulations. And full numerical details and discretization methods are presented in Table 3.

4. Results and discussion

4.1. Validation of predicted flow characteristics

The CFD methodology is used for near-saturated flow boiling of FC-72 under near- microgravity ($g \sim 0.05\ m^2/s$, opposite to the flow direction) for the three sets of operating conditions indicated in Table 1. The inlet thermodynamic equilibrium quality is calculated according to

$$x_{e,in} = \frac{h_{in} - h_f}{h_{fg}} = -\frac{c_{p,f}(T_{sat} - T_{in})}{h_{fg}}, \tag{7}$$

where $c_{p,f}$, T_{sat} and h_{fg} are based on measured inlet pressure, P_{in}, while inlet temperature, T_{in}, is measured by the thermocouple up-

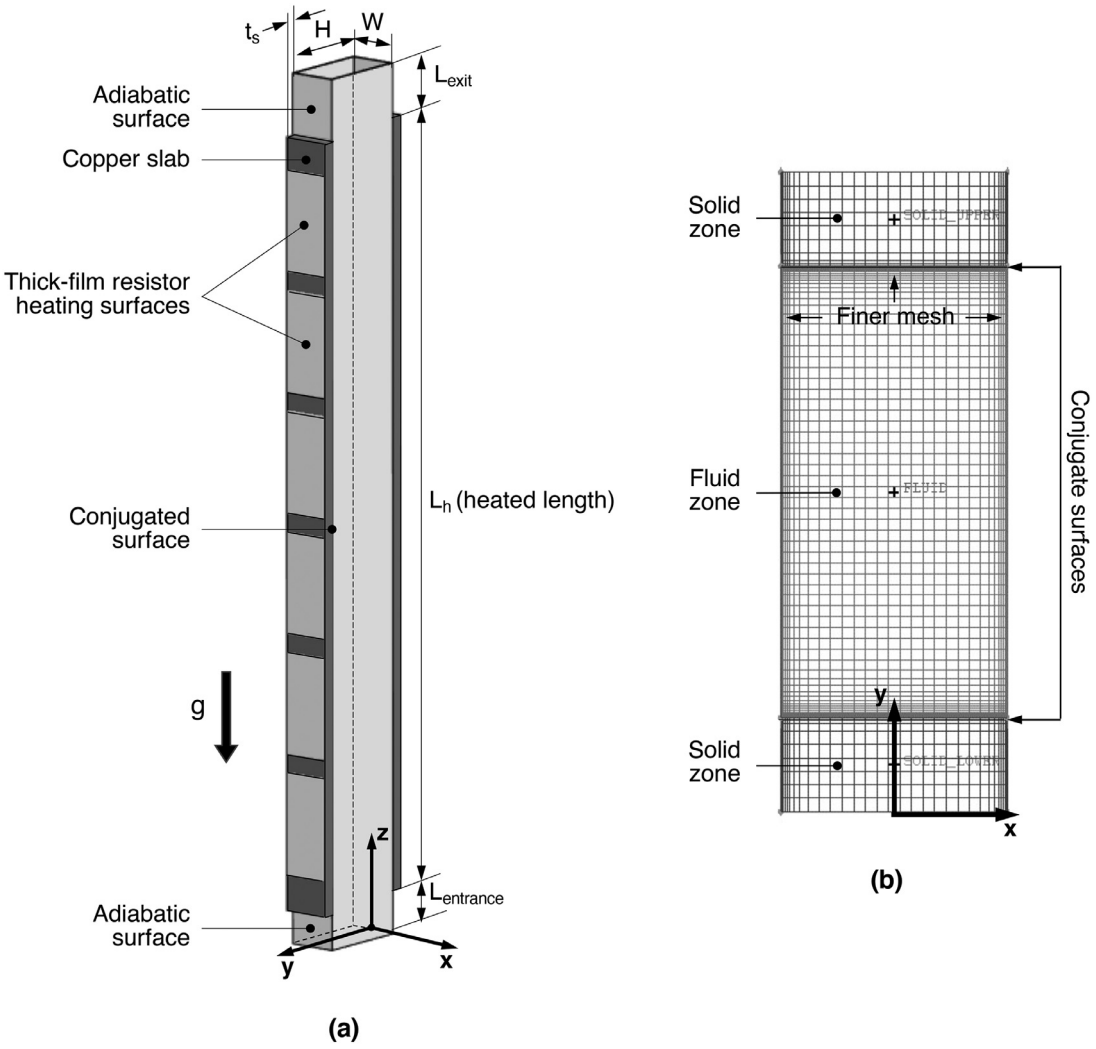

Fig. 4. (a) 3D computational domain. (b) Mesh details.

Table 1
Experimental operating conditions for three test cases modeled numerically.

Test case	P_{in} (kPa)	T_{sat} (°C)	$\Delta T_{sub,in}$ (°C)	$x_{e,in}$	G (kg/m^{2}s)	q'' (kW/m^2)
1	120.3	62.1	5.1	−0.07	200.5	75.1
2	130.0	64.4	6.2	−0.09	444.1	176.0
3	133.4	65.3	5.7	−0.07	758.9	193.1

Table 2
Thermophysical properties used in computational model.

Test case	T_{sat} (°C)	h_{fg} (J/kg mol)	ρ_f (kg/m^3)	$c_{p,f}$ (J/kg·K)	k_f (W/m·K)	μ_f (kg/m·s)	ρ_g (kg/m^3)	$c_{p,g}$ (J/kg·K)	k_g (W/m·K)	μ_g (kg/m·s)	σ (N/m)
1	62.1	2.773×10^7	1608.8	1117.5	0.0536	3.848×10^{-4}	15.966	942.70	0.0142	1.210×10^{-5}	0.0080
2	64.4	2.749×10^7	1602.4	1122.4	0.0533	3.731×10^{-4}	17.164	950.69	0.0144	1.220×10^{-5}	0.0078
3	65.3	2.750×10^7	1602.4	1122.4	0.0533	3.732×10^{-4}	17.157	950.65	0.0144	1.220×10^{-5}	0.0080

Table 3
Numerical details and discretization methods.

Pressure-velocity coupling	Pressure-implicit with splitting of operators (PISO)
Gradient	Least square cell based
Pressure	PRESTO!
Momentum	Third-order monotonic upstream-centered scheme for conservation laws (MUSCL)
Volume fraction	Geo-reconstruct
Turbulent kinetic energy	Second-order upwind
Specific dissipation rate	Second-order upwind
Energy	Second-order upwind
Transient formulation	First-order implicit

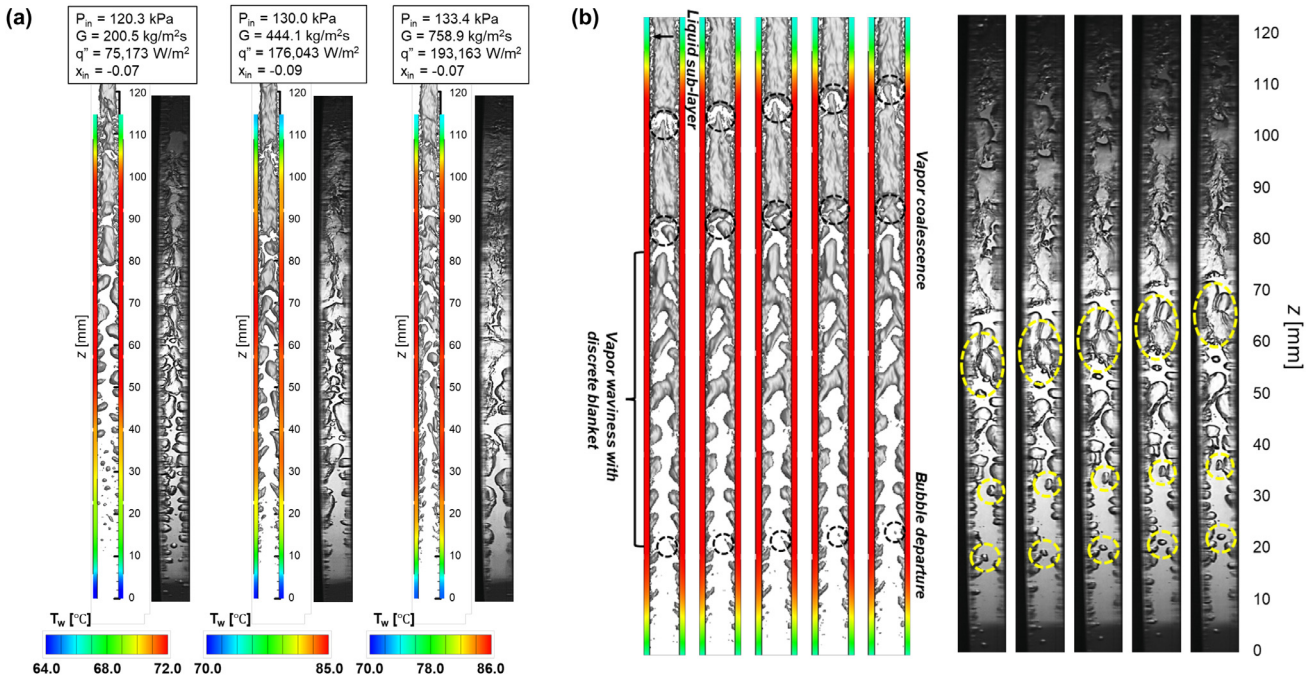

Fig. 5. (a) Comparison of flow visualization from experiments with predictions of 3D CFD method shown along with axial variations of predicted wall temperature. (b) Sequential images separated by 1 ms captured from computations and experiments for the intermediate case of $G = 444.1$ kg/m^{2}s and $q'' = 176{,}043$ W/m^2.

stream of the test section. The present CFD methodology has already been validated for subcooled vertical upflow boiling in Earth gravity [41–43]; the results presented here are intended to validate the same methodology for near-saturated conditions and absence of body force.

In terrestrial environment, boiling is highly influenced by large density difference between liquid and vapor, which yields a buoyancy force that can have a profound influence on flow structure and therefore heat transfer. Overall, flow structure is dictated by the net effect of (i) body force, (ii) flow inertia, and (iii) surface tension force. For vertical upflow in terrestrial gravity, buoyancy force parallel to the heated walls has weaker effect on vapor bubble migration toward the core compared to other orientations, but it has significant influence on bubble growth, which is implicit in the influence on drag and lift forces.

But, in microgravity, absence of body force implies flow structure is the outcome of combined effects of only flow inertia and surface tension. Here, experimental measurements and video motion analysis from parabolic flight experiments play primary roles in assessing the effectiveness and accuracy of the same CFD approach in tackling microgravity.

Fig. 5(a) shows, for the three test cases, comparisons of computationally determined two-phase flow structure with that captured with video, as well as predicted wall temperature variations along the channel. The individual images illustrate instantaneous and temporal tracking of the interfacial behavior after steady state is achieved. The vapor is captured from the iso-surface of $\alpha_g = 0.5$, which represent the exact middle between liquid and vapor phases. Notice how bubble nucleation commences at the leading edge of the heated length because wall temperature is higher than saturation temperature at corresponding operating pressure. Massive nucleation is shown taking place in the middle of the heated length where the difference between local and saturation temperature is largest. However, due to decreasing volume of fraction of the liquid phase, the amount of evaporation levels off farther downstream. Predicted flow regimes mimic well those captured with high-speed video.

Fig. 5(b) shows sequential images captured from computational and experimental methods to illustrate the dynamic process of flow boiling. The time interval between images is 1-ms for both. Key flow boiling features are (i) bubble growth, (ii) bubble coalescence, (iii) initiation of coalescent, discrete wall vapor blankets, (iv) interfacial waviness of vapor blankets, (v) blanket merger, and (vi) residual liquid sub-layer beneath vapor blankets responsible for cooling of the wall, especially downstream. As essential interfacial features are determined from velocity field computed from the momentum equation, it is important to appropriately model forces acting on interface. Notice that all these flow features are both evident in the video images and captured in the computed interfacial structure. For all three cases, a bubbly flow pattern is observed upstream, with bubbles initially confined to the heated wall, but gradually increasing in size due to both increased evaporation and coalescence, causing vapor to gradually penetrate farther into the core. Vapor bubbles are detached from one another following severe deformation and breakup. This is followed downstream by formation of oblong coalescent vapor structures resembling discrete vapor blankets. A liquid sublayer is observed in computed results residing beneath the discrete vapor blankets, providing wall cooling downstream. The flow downstream appears nearly annular.

The variations of predicted wall temperature in Fig. 5 illustrate several noteworthy trends. First, wall temperature is lowest near the inlet because of abundant liquid access and contributions of both latent and some sensible heat, the latter is relatively small because of low subcooling of incoming fluid. The liquid access in gradually compromised along the channel, causing a monotonic axial increase in wall temperature to a rather uniform level near the middle before subsiding in the downstream unheated region.

Overall, the CFD predictions of the flow structure generally mirror those captured with video. However, there are differences in certain local features. For example, the video images show more appreciable bubble growth in the upstream region, which also causes earlier vapor coalescence, deeper penetration into the core, and earlier formation of discrete vapor blankets. In addition, full

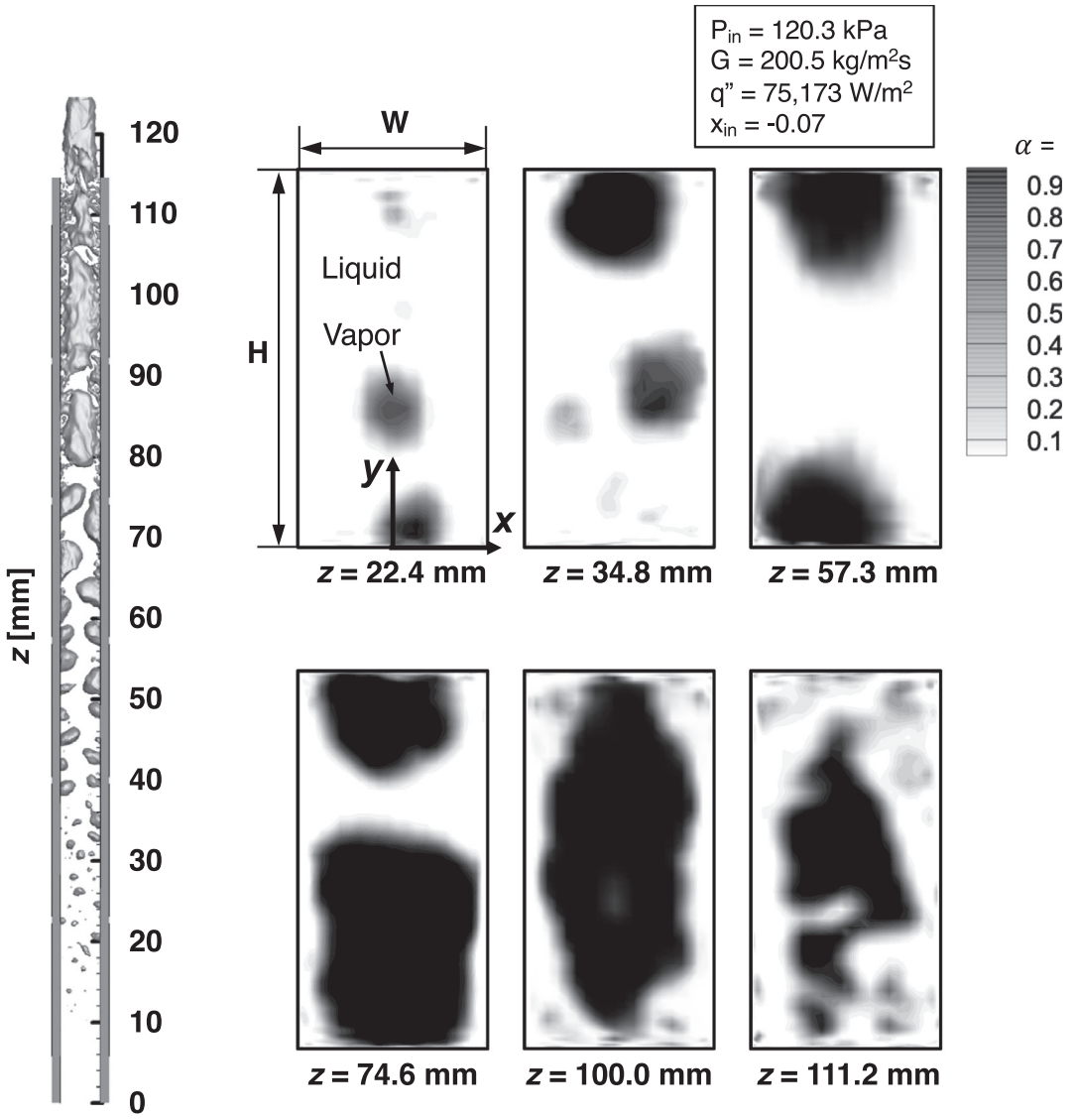

Fig. 6. Vapor formations in the channel's cross-section computed at six axial locations.

growth of vapor bubbles in the simulations is limited by undeveloped thermal boundary layer. Some of these deviations can be attributed to differences related to coalescence between bubbles. More specifically, bubbles in experiment at times approach one another but do not coalesce into a larger bubble. This is captured in the video image for $G = 200.5$ kg/m^{2}s, where bubbles are seen touching one another while moving downstream, but not merging. On the other hand, bubbles in the simulations are shown coalescing once they touch. Combination of the VOF and surface tension models used in the present CFD method provides reliable results in situations where discrete bubbles are perfectly surrounded by liquid, but is less accurate, for example, when two bubbles are very close to one another, which causes touching between the numerically diffused interfaces.

4.2. Hydrodynamics of flow boiling in microgravity

A key advantage of the CFD method is ability to capture two-phase flow features that are impossible to capture via video without some sort of stereoscopic viewing system, and bubble shape and evolution data would be limited at best in a plane normal to flow direction. Fig. 6 shows computed images of vapor bubble formation in the channel's cross-section (x-y plane) at six axial locations of $z = 22.4$, 34.8, 57.3 , 74.6 , 100.0 , 111.2 mm, shown here for the lowest mass velocity case. Also included for reference are axial variations of flow structure from Fig. 5. In Fig. 6, instead of using a threshold of $\alpha_g = 0.5$ (exact middle of interface as shown in Fig. 5), a volume-of-fraction for vapor between 0 and 1 is used to capture any local features around vapor bubbles and heated walls after steady state is achieved.

Several noteworthy vapor features are captured within the cross-section for the different axial locations. First, for $z = 22.4$ and 34.8 mm, bubbles appear adhering to the heated wall because of strong surface tension effects. Bubble shape for the first two regions points to growth of mostly single bubbles rather than to bubble coalescence. The coalescence is more evident at $z = 57.3$ mm; this is where the longitudinal flow pattern depicts discrete wavy vapor blankets on the opposite heated walls approaching one another, aiming for merger across the core. Vapor begins to depart from the heated wall at $z = 74.6$ mm. At $z = 100.0$ mm, the merger has occurred, but liquid is still available around the entire circumference, providing residual cooling to both heated walls. Liquid fills the wall vicinity more aggressively due to recirculation resulting from interfacial and wall shear stresses during vapor bubble

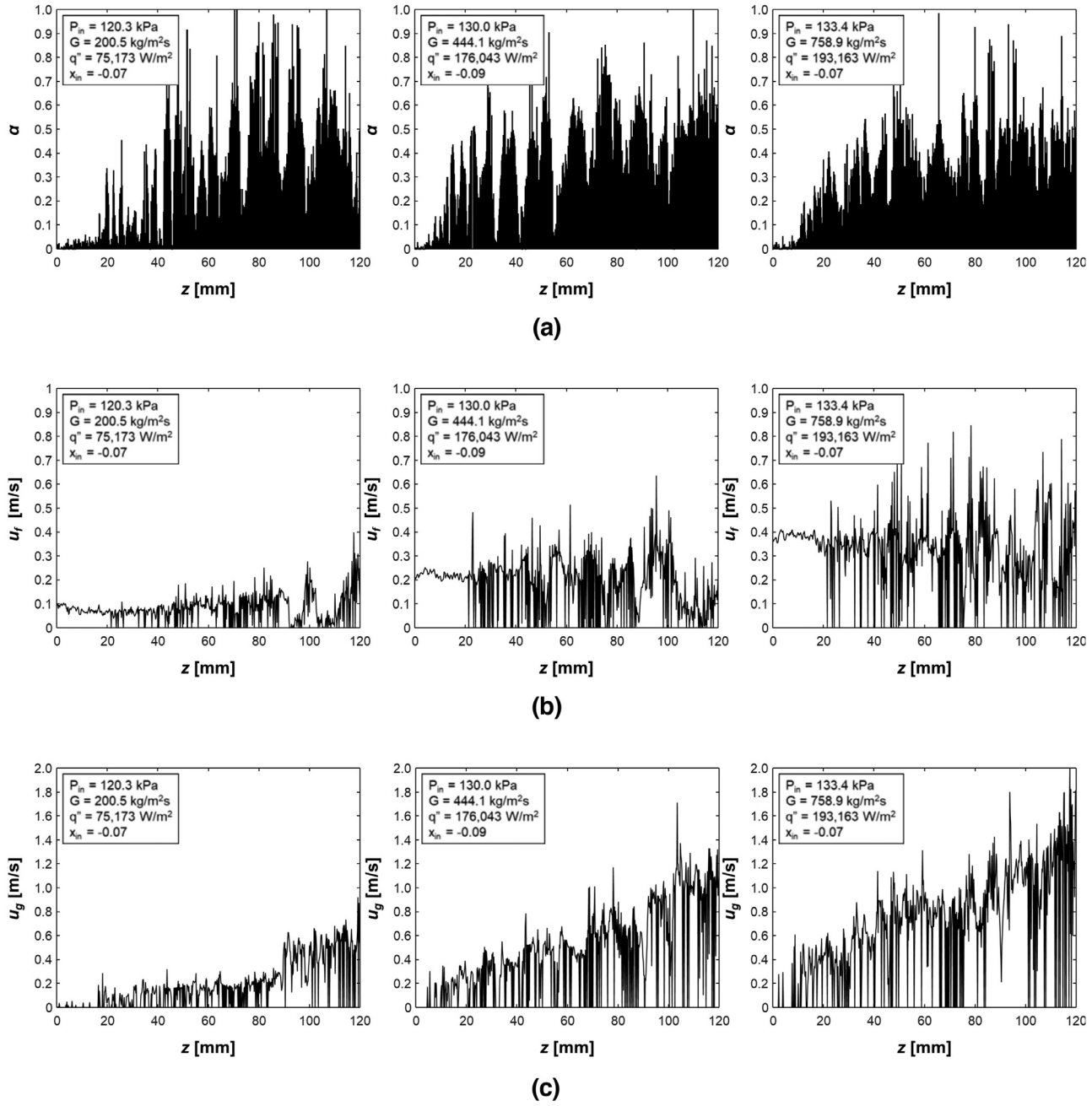

Fig. 7. Axial variations of instantaneously computed (a) vapor fraction, (b) liquid velocity, and (c) vapor velocity for three test cases.

departure. The liquid takes the form of a liquid sub-layer, which may encourage some additional nucleation, as captured in the longitudinal view. Note that local small features within the liquid layer, especially bubble nucleation and departure, are evident in the cross-sectional views at $z = 100.0$ and 111.2 mm. At $z = 111.2$ mm, the large coalescent vapor mass in the core incurs appreciable deformation and breakup, which can be attributed to increased inertia, outcome of vapor acceleration along the channel, as compared to surface tension, and increased turbulence. Here too, the α_g threshold prevents capture of small near-wall nucleation features.

Fig. 7 shows another advantage of the CFD method: ability to capture detailed axial variations of void fraction, α, liquid velocity, u_f, and vapor velocity, u_g. Each of these variables is spatially and volumetrically averaged from cells in the x-y plane (channel cross-section). For the cases of slug or annular flows or bubbly flow with multiple fully entrained vapor bubbles, $\alpha = 0.5$ provides a reasonably accepted location for interface position. However, as presented in Fig. 6, for small vapor bubbles which are (i) beginning to lift from the wall but are not fully grown or (ii) separated from larger vapor bubbles due to bubble breakup, α does not approach unity. With α unable to span the entire 0–1 range, using the criterion of $\alpha = 0.5$ to identify interface position is simply not applicable to these small bubbles. Therefore, the threshold of $\alpha = 0.9$ is adopted in the present study to identify the vapor phase. Fig. 7(a) shows variation of void fraction along the channel. The α values are quite low in first 10–15 mm, corresponding to the slightly subcooled boiling region. With gradual evaporation, especially downstream, α is shown increasing rapidly for all three cases. For reference, simple energy balance calculations show the upstream sub-

cooled region terminates roughly at the axial location corresponding to thermodynamic equilibrium quality of $x_e = 0$, $z = 38.3$, 44.1, and 63.2 mm for $G = 200.5$, 444.1, and 758.9 kg/m^{2}s, respectively.

Fig. 7(b) shows axial variations of u_f for the three test cases. Notice how u_f is somewhat constant in the upstream 20 mm from the entrance because of small volume of vapor produced in this region. Farther downstream, u_f begins to experience large fluctuations, with high peaks resulting from the large increase in α. There are also severe depressions in u_f between peaks, which are brought about by the liquid-sublayer portions of the cross-section between the large discrete vapor blankets. In the exit region in particular, the liquid layer is affected by the non-slip condition from the wall as vapor core engulfs most of the channel, resulting in low liquid velocity.

Fig. 7(c) shows axial variation of u_g for the three test cases. Notice the appreciable axial increase in u_g, indicative of massive acceleration of the vapor, which is also reflected in the large axial increase in α. Shown is a rather monotonic increase in u_g, along with severe fluctuations, especially for the intermediate and highest mass velocities. Notably, peak values for u_g are around 5 times higher than the liquid inlet ($u_{f,in} = 0.12$, 0.27, 0.47 m/s for $G = 200.5$, 444.1, and 758.9 kg/m^{2}s, respectively).

It is important to note that no modifications to the CFD methodology are required to simulate flow boiling in microgravity. The main difference is that, unlike simulations in terrestrial gravity, the body force term in the momentum equation is negligibly small and the convection term (which dictates time-dependent velocity changes) is balanced by the diffusion and pressure gradient terms. To assess how absence of body force influences two-phase structure, it is useful to compare computed interfacial behavior in microgravity to that from the authors' prior work [43] (which also uses $r_i = 100$ s^{-1} for evaporation and 0.1 s^{-1} for condensation) involving vertical upflow in terrestrial gravity. Such comparison is shown in Fig. 8, with the channel tilted slightly to better display bubble formation along one of the heating walls, and only portions of the heated portion of the channel (entrance, middle, and exit) presented. The microgravity case corresponds to the intermediate mass velocity of $G = 444.1$ kg/m^{2}s and 69% CHF. For comparison, the terrestrial case corresponds to a fairly similar mass velocity (445.7 kg/m^{2}s) and 78% CHF (nearest value available from the prior study). Note the substantial differences between the heat flux values (176,043 versus 278,705 W/m^2) which are attributed to appreciably lower CHF for microgravity compared to that for the terrestrial case. A key difference between the two gravity levels is ability of body force in Earth gravity to assist earlier vapor bubble removal and contribute appreciable acceleration to the two-phase flow. On the other hand, Fig. 8 shows absence of body force in microgravity allows bubbles to reside longer along the heated walls and grow bigger before departure. Large bubbles in microgravity also contribute increased bubble coalescence into fairly large blankets in the middle section, culminating in the vapor engulfing much of the cross-section in the exit section, which also explains the lower CHF value. One might also extrapolate that the differences in flow structure and CHF between the two gravity levels would diminish monotonically with increasing G, becoming nearly identical at very high G, as inertia dwarf any body force effects.

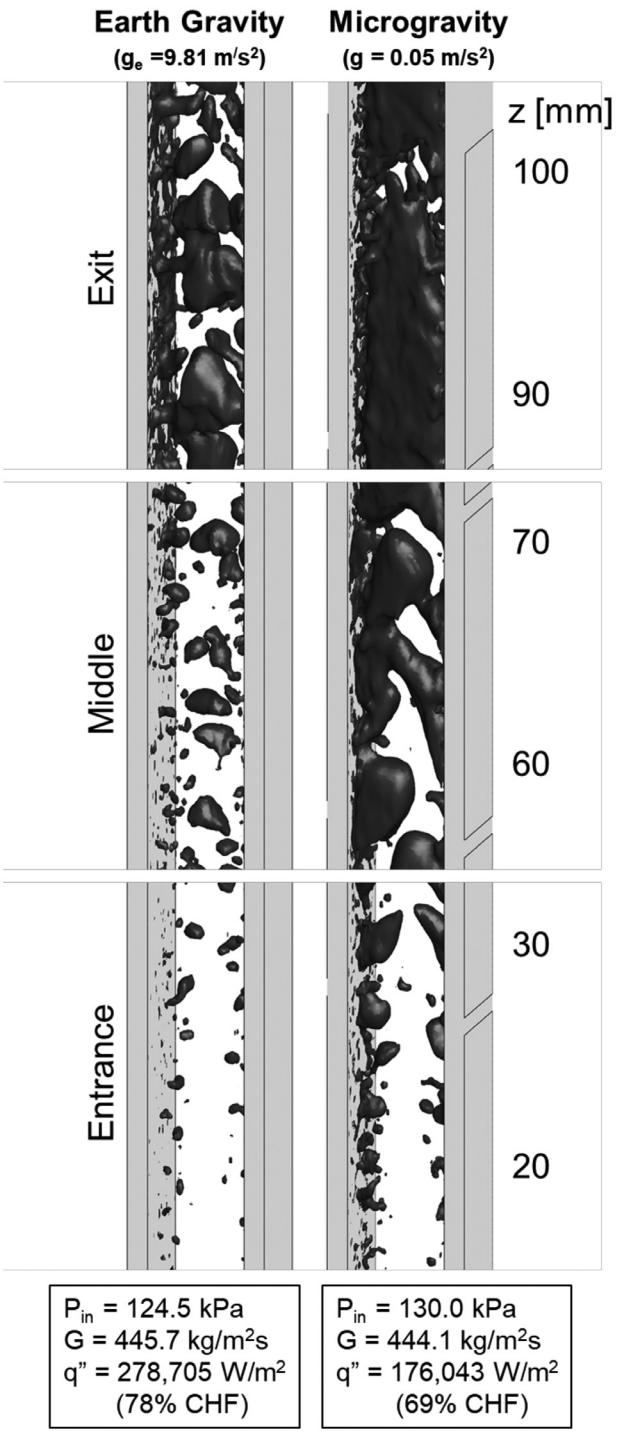

Fig. 8. Computed two-phase flow structure in vertical upflow in Earth Gravity versus microgravity.

4.3. Heat transfer characteristics concomitant with aggressive vapor generation

Fig. 9 shows predicted axial variations of both surface heat flux, $\bar{q}''$, and void fraction averaged across the transverse x-direction directly on one of the heated walls. The heat flux is defined here as that passing through interface between solid and fluid. Most noticeable in Fig. 9 is the direct correspondence between surface heat flux and void fraction along the flow direction for each of the three test cases. The heat flux is quite small in the inlet region where heat transfer is impacted by single-phase liquid convection, given the smaller number of active nucleation sites. Notice that heating along the wetted surface of the copper slab is concentrated around regions corresponding to location of the thick film resistors. With the most upstream resistive heater starting at 5.85 mm from the inlet, heat flux is quite small up this axial location. Weak bubble activity in the same region helps explain low values of void fraction as well. Downstream of $z = 22$ mm, both the sur-

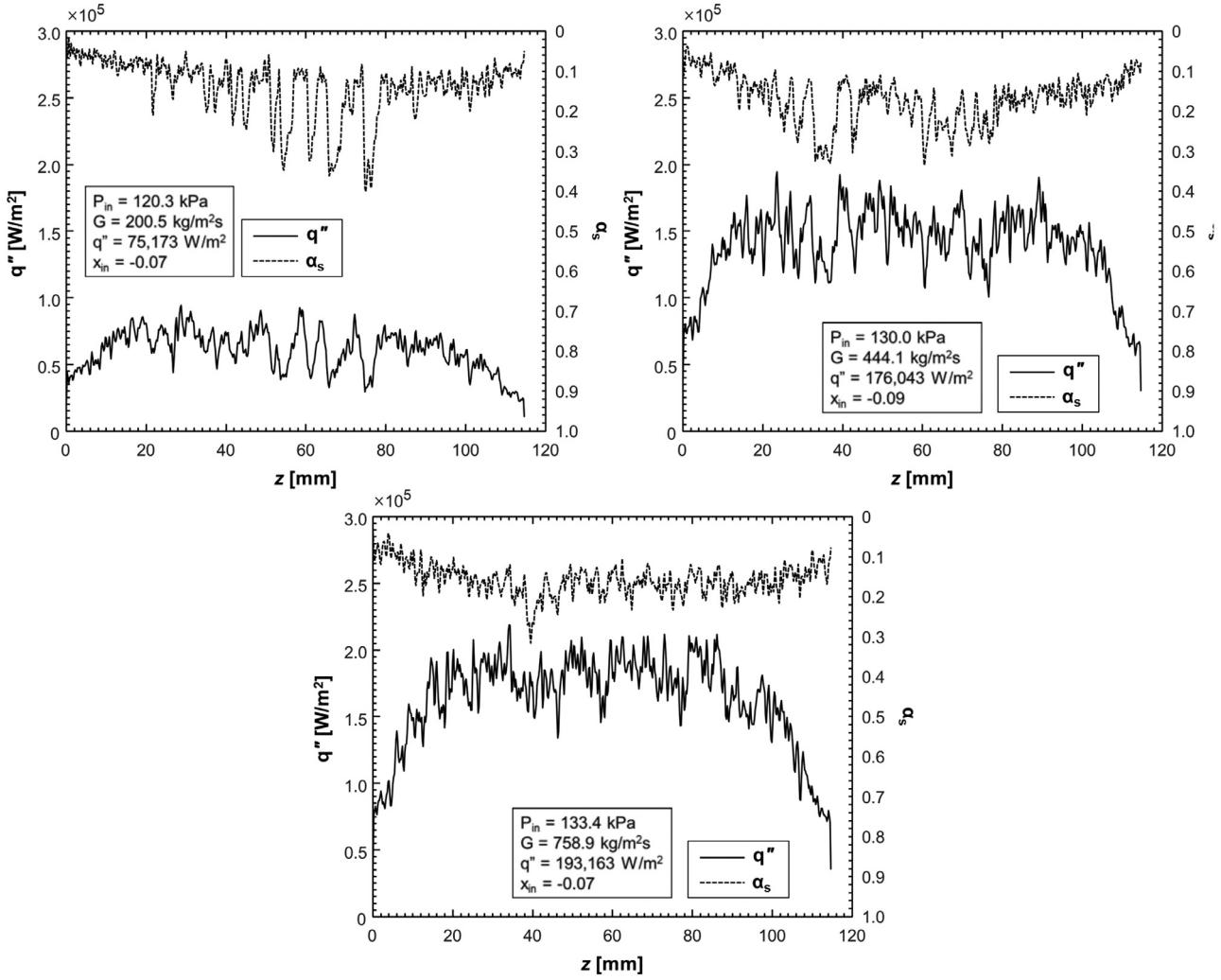

Fig. 9. Axial variations of instantaneously computed surface heat flux and void fraction, both averaged over transverse *x*-coordinate for same heated wall.

face heat and void fraction increase appreciably and experience severe fluctuations stemming from complex changes in interfacial activity, including bubble formation, growth, and departure, as well as eventual bubble coalescence and vapor blanket formation. Interestingly, z locations of minimum surface heat flux during these fluctuations coincide with maximum values of void fraction. Surface heat flux minima are presumably the result of large coalescent bubbles forming locally at the heated wall, and maxima where the same bubbles depart, inducing wall replenishment by bulk liquid. This same bubble activity helps explain the opposite trends in fluctuation maxima and minima of surface heat flux and void fraction. Farther downstream, surface heat flux subsides appreciably because of (i) appreciable vapor blanketing and (ii) unheated downstream 5.85 mm of the copper slab length (downstream edge of most downstream resistive heater is located at $z = 108.75$ mm from the inlet).

Fig. 10 shows computed fluid mixture temperature, T_m, in heated portion of the flow channel for the three test cases. These contour plots are captured instantaneously from center plane (y-z plane) at $x = 0$. As mentioned earlier, all three conditions involve slightly subcooled inlet conditions, and saturation temperatures corresponding to $G = 200.5$, 444.1, and 758.9 kg/m^{2}s are $T_{sat} = 62.1$, 64.4, and 65.3, respectively. As expected, subcooled core fluid penetrates farther downstream with increasing G, and near-wall fluid in the upstream region is saturated or slightly superheated for all three cases but shows highest downstream superheating for the lowest G.

Fig. 11 compares axial variations of numerically computed and analytically calculated average fluid temperature, $\bar{T}_m$. Here, computed temperature from the computational approach is a volume-weighted average over the cross-sectional area, while the analytically estimated temperature is based on inlet and outlet measured fluid temperature and pressure. The analytically calculated values account for axial variations of saturation temperature resulting from pressure drop across the heated portion of the channel, which is assumed to be linear. Both calculated thermodynamic equilibrium quality and fluid temperature are calculated from a simple energy balance considering heat input from the heated walls. To estimate fluid temperature along the heated length, a simple energy balance is adopted. Calculation of fluid temperature upstream of the location where thermodynamic equilibrium quality, x_e, equals zero is based on sensible heat gain. But, for downstream locations where $0 < x_e < 1$, local fluid temperature is set equal to saturation temperature corresponding to local pressure. The computed fluid temperature in simulations reflects the expected nearly linear trend in the upstream subcooled region ($x_e < 0$), followed by near saturated temperature where $x_e > 0$. For all three test cases, Fig. 11 shows good agreement between numeri-

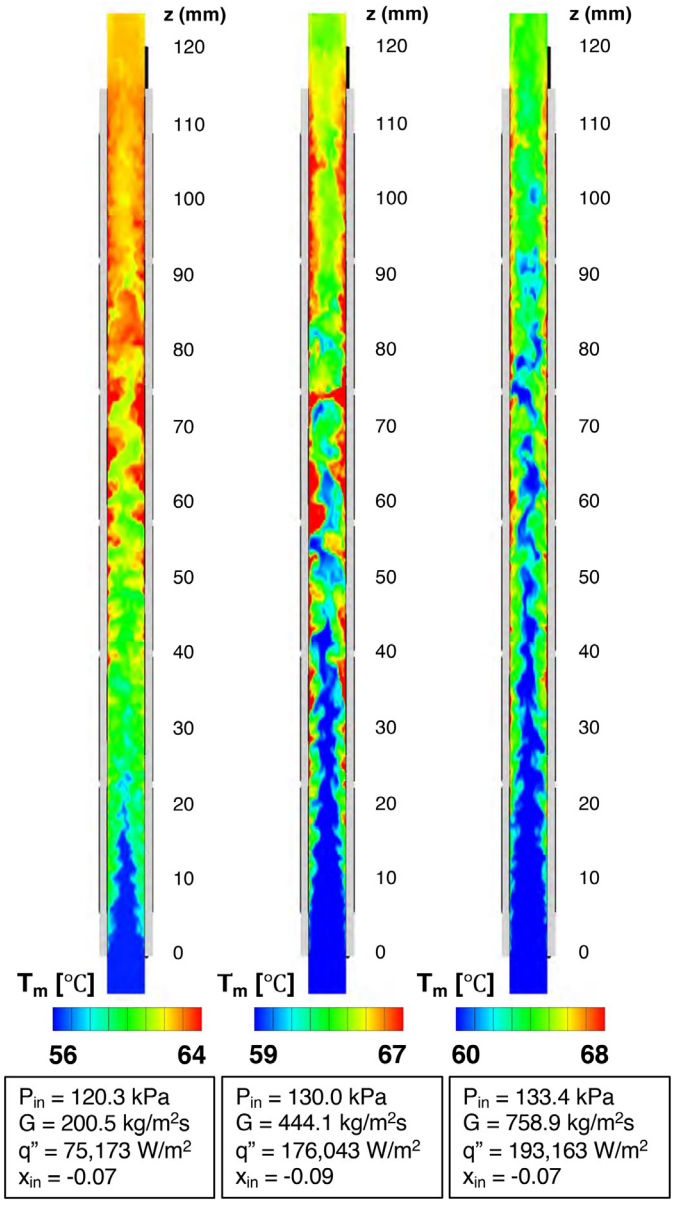

Fig. 10. Computed fluid mixture temperature in heated portion of the flow channel for the three test cases.

cally computed and analytically calculated fluid temperatures, especially in the inlet and outlet regions. Absent in the calculated temperatures, however, is the sharp decrease in slope in the middle region. This can be explained by the fact that the analytical estimations are based entirely on idealized thermodynamic equilibrium quality assumptions, whereas the computed values account for realistic non-equilibrium effects.

Fig. 12 compares axial variations of computed and measured wall temperatures for the three test cases and two heating walls. The wall temperatures are measured by thermocouples embedded in the copper slabs at z = 5.4, 22.7, 40, 57.3, 74.6, 91.9, and 109.2 mm. Computed values in this figure are space- and time-averaged over periods when CFD results reach steady state. Several important observations are readily apparent from these plots. First, computed wall temperature plots for the two walls are virtually identical, so are the measured wall temperatures. Second, computed wall temperature increases in the entrance region (z = 0–22 mm), especially for the two higher mass velocities, result of

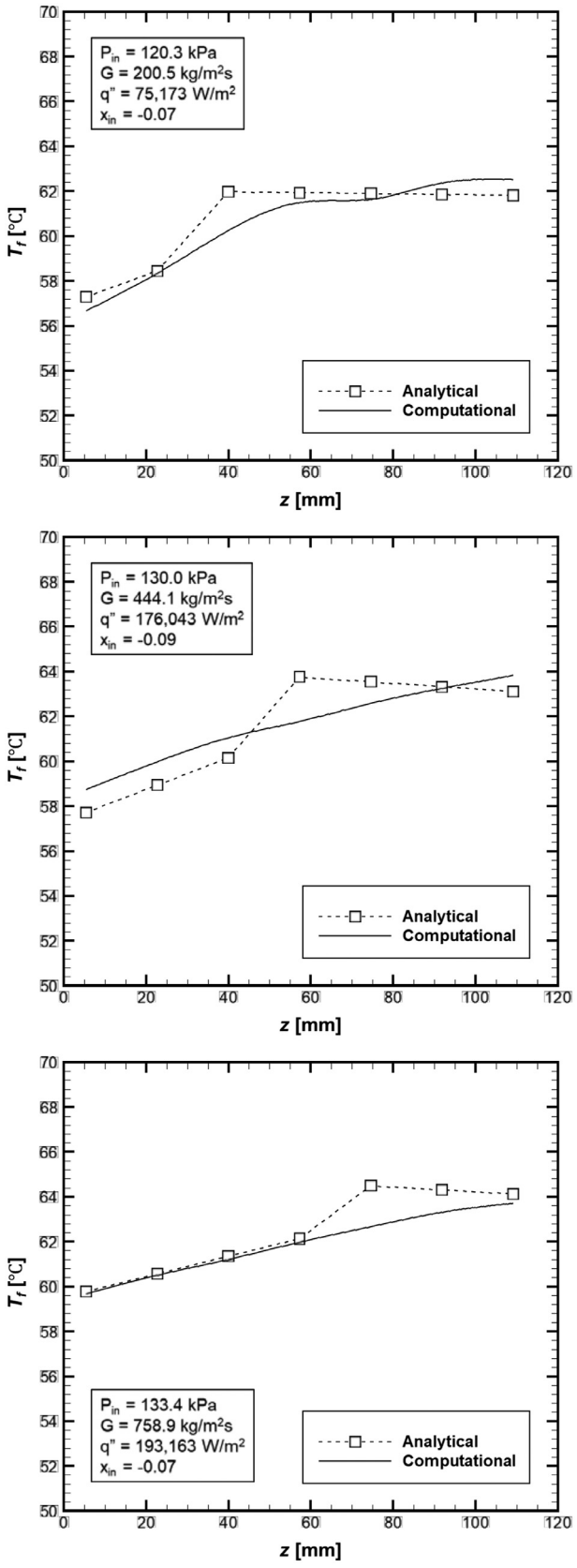

Fig. 11. Comparison of axial variations of computed and calculated average fluid temperatures.

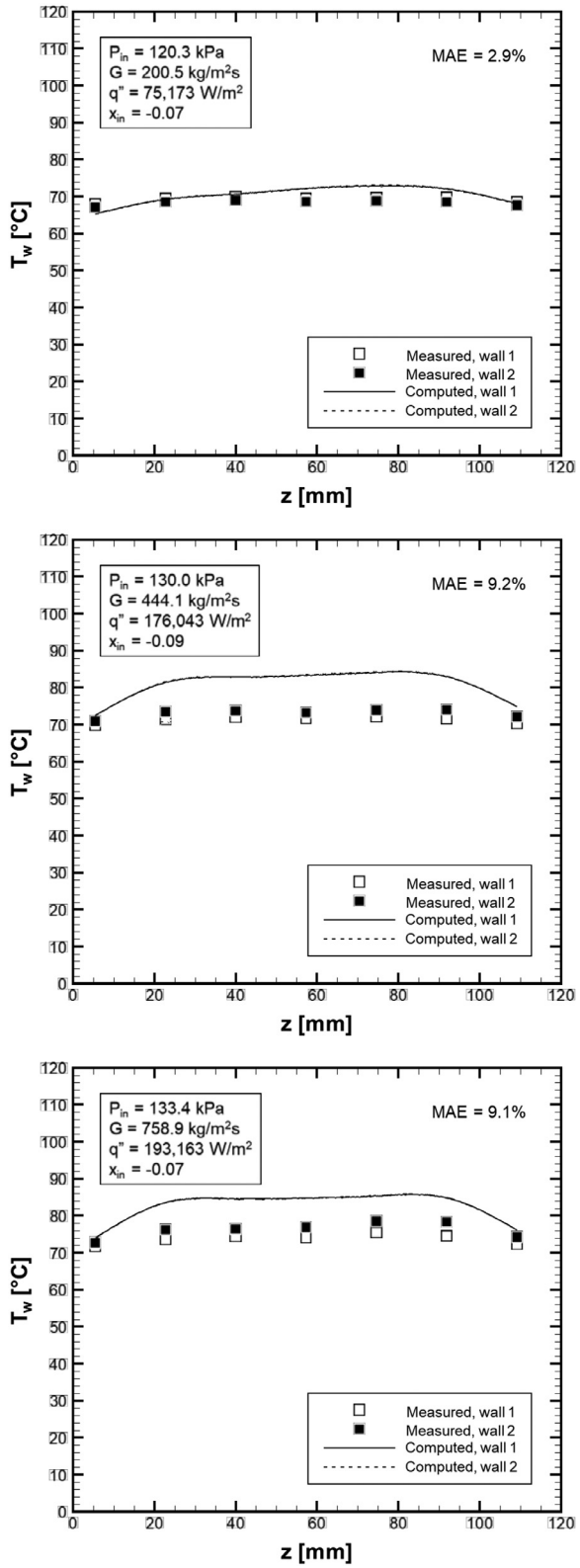

Fig. 12. Comparison of axial variations of computed and measured wall temperatures for three test cases.

the strong contribution of sensible heat transfer to liquid in this region and presence of a short unheated length upstream. The increase is more pronounced for the computed temperatures. Third, both computed and measured plots are nearly flat in the middle region, where nucleate boiling is well developed, as shown earlier in Fig. 5. For the computed plots, wall temperatures in the middle region are about 71, 82 and 84 °C for $G = 200.5$, $G = 444.1$, and $G = 758.9$ kg/m^{2}s. Clearly temperature differences are the outcome of not only mass velocity but heat flux as well. Fourth, the computed wall temperatures decrease in the exit region (from $z \sim 90$ mm), especially for the two higher mass velocities, a result of compromised cooling resulting from newly generated nucleation within the liquid sub-layer beneath large vapor blankets and presence of a short unheated length downstream. Moreover, because of both gradual fluid temperature rise and vapor layer development, flow is gradually accelerated toward the exit, helping to enhance heat transfer. Like the entrance region, this effect is more pronounced for computed compared to measured temperatures.

Overall, it is obvious that the CFD method provides fairly reasonable predictions of wall temperature, evidenced by a difference (overprediction) of ~ 3 and ~ 10 °C for the lowest and the two highest mass velocities. In general, numerical prediction of subcooled boiling is very challenging because of non-equilibrium effects, which compromises ability to accurately account for heat removal by subcooled liquid filling the wall vicinity after bubble detachment. To improve the microgravity predictions, variations in the value of mass intensity factor, r_i, (especially for evaporation) in the Lee model [46] might be attempted. Furthermore, the volume of fraction in CFD is a continuous function of time and space, which is intended to avoid sharp discontinuity that cannot be differentiated close to the Heaviside step function in the actual situation ($\alpha_g = 0$ for liquid and $\alpha_g = 1$ for vapor). Due to inborn limitations of the numerical and mathematical approaches used, values of volume of fraction for each phase are between 0 and 1, leading to some deviations in terms of computing mass transfer rate, heat removal, and mechanical properties. Additional deviations can be attributed to inability of the two-equation turbulence model to account for anisotropic effects around the interface.

Finally, Fig. 13 provides, for the middle G case, important insight into transport characteristics in the near-wall region ($y = 0$ – 0.4 mm, essentially within the liquid sub-layer) at a downstream location of $z = 91.9$ mm, information that is extremely difficult to measure experimentally. This includes computed turbulence dissipation rate, ε, dimensionless temperature profile, $T^* = (T - T_{sat})/(T_w - T_{sat})$, mass transfer rate, Γ, and axial velocity of mixture, u_z, presented in Fig. 13(a) to (d), respectively, with void fraction, α, superimposed in each figure for reference. These profiles are instantaneously exported after steady state along $x = 0$ for each y location.

Turbulent dissipation rate, ε, and turbulent Prandtl number are two parameters whose values are crucial to accurate determination of temperature profile across the liquid film. For an idealized configuration of a thermally developed liquid film, heat flux across the film is equal to the applied wall heat flux. According to prior work [43], constant heat flux implies the slope of temperature profile across the film is large where ε tends to zero (in the viscous very-near-wall region of the film), and small where ε is large. These trends are evident when comparing the ε profile in Fig. 13(a) with the corresponding temperature profile in Fig. 13(b). However, this relationship is complicated by the fact that the liquid film is not continuous but punctured at the wall by nucleating bubbles. This is manifest in Fig. 13(a), which shows void fraction is small very close to the heated wall but increases dramatically due to the bubble nucleation within the liquid film, then decreases within the liquid until $y \sim 0.2$ mm before increasing again to $\alpha \sim 1$ in the vapor core. The increase in ε away from the wall is attributed to increased turbulent mixing in the axially accelerating vapor core. Fig. 13(c) shows mass transfer rate, Γ, is highest near the wall due to liquid film evaporation but subsides appreciably toward the vapor core. Finally, Fig. 13(d) shows axial velocity is zero at the wall (no-slip boundary) and increases appreciably toward the vapor core.

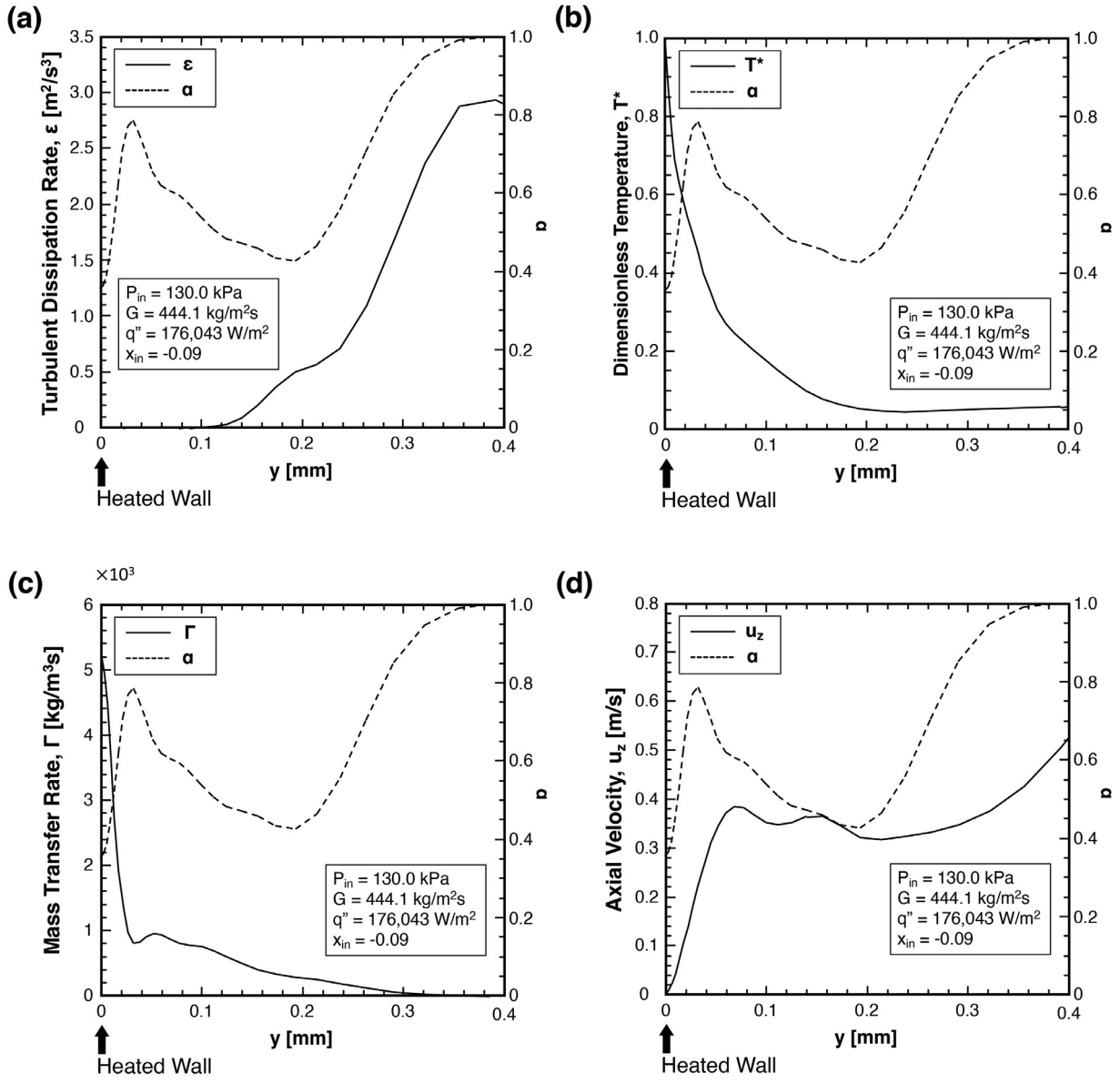

Fig. 13. Near-wall profiles of (a) turbulent dissipation rate, (b) dimensionless temperature, (c) volumetric mass transfer rate, and (d) axial velocity, computed at $z = 91.9$ mm for $G = 444.1$ kg/m^{2}s and $q'' = 176{,}043$ W/m^2.

5. Conclusions

The present study focused on use of Computational Fluid Dynamics (CFD) to predict near-saturated flow boiling of FC-72 in microgravity. The computational method provided detailed 3D predictions of interfacial behavior and heat transfer characteristics along a rectangular channel heated along two opposite walls. The method used is based on the multi-phase volume of fluid (VOF) model, which is combined with appropriate phase change and turbulence models, and accounts for both shear-lift force on bubbles and conjugate heat transfer along the heating walls. Validation is achieved by comparing predictions to experimental wall temperature measurements and high-speed video images captured during a series of parabolic aircraft maneuvers. Key findings from the study are as follows:

(1) Use of the CFD method with shear-lift force modeling predicts flow boiling in microgravity with reasonably good agreement with experiment. In the condition with almost absence of gravitational acceleration, bubbles are bigger and flow pattern evolves differently along the heated length compared to that for terrestrial gravity from prior work. In Earth gravity, buoyancy promotes earlier vapor bubble removal and contributes appreciable axial acceleration to the two-phase flow. On the other hand, microgravity causes bubbles to reside longer along the heated walls and grow bigger before departure. Large bubbles in microgravity also contribute increased bubble coalescence into fairly large vapor blankets downstream.

(2) Due to appreciable sensible heat transfer in the upstream region, growth of mostly single bubbles is more prevalent than coalescence. The bubble coalescence intensifies in the middle of the heated portion of the flow channel where discrete wavy vapor blankets on the opposite heated walls exist. Farther downstream, appreciable vapor coalescence engulfs the channel's core region while liquid is still available around the entire circumference, providing additional nucleation.

(3) Non-equilibrium effects are evident in the subcooled liquid region and also reflected in intermittent superheating of the vapor blankets, resulting in minor deviations of fluid temperature

from simulations compared to those predicted by the analytical method. Predicted wall temperature is fairly uniform in the middle of the heated length but increases in the entrance region, due to sensible heat transfer in the subcooled liquid, and decreases toward the exit, mostly because of flow acceleration resulting from increased void fraction.

(4) Inaccuracies posed by the adopted VOF and surface tension models are attributed to situations involving vapor bubbles in close proximity to one another. In this situation, numerically diffused interfaces might trigger premature touching between the bubbles and contribute errors in prediction of flow regimes and their transitions.

Declaration of Competing Interest

None, The authors declare that they have no known competing financial interests or personal relationships that could have appeared to influence the work reported in this paper.

Acknowledgment

The authors are grateful for financial support provided by the National Aeronautics and Space Administration (NASA) under grant no. NNX17AK98G, and support from FBCE project of the NASA Glenn Research Center.

References

[1] F.P. Chiaramonte, J.A. Joshi, Workshop on critical issues in microgravity fluids, transport, and reaction processes in advanced human support technology, NASA, 2004 final report TM-2004-212940.
[2] National Research CouncilRecapturing a future for space exploration: Life and physical sciences research for a new era, National Academies Press, Washington, DC, 2011.
[3] T.J. LaClair, I. Mudawar, Thermal transients in a capillary evaporator prior to the initiation of boiling, Int. J. Heat Mass Transf. 43 (2000) 3937–3952.
[4] Y. Abe, A. Iwasaki, Pool boiling under microgravity, Adv. Space Res. 13 (1993) 165–168.
[5] H. Merte, Momentum effects in steady nucleate pool boiling during microgravity, Ann. N.Y. Acad. Sci. 1027 (2004) 196–216.
[6] H. Merte, Some parameter boundaries governing microgravity pool boiling modes, Ann. N.Y. Acad. Sci. 1077 (2006) 629–649.
[7] H. Zhang, I. Mudawar, M.M. Hasan, Experimental and theoretical study of orientation effects on flow boiling CHF, Int. J. Heat Mass Transf. 45 (2002) 4463–4477.
[8] C. Konishi, I. Mudawar, Review of flow boiling and critical heat flux in microgravity, Int. J. Heat Mass Transf. 80 (2015) 469–493.
[9] I. Mudawar, R.A. Houpt, Mass and momentum transport in smooth falling liquid films laminarized at relatively high Reynolds numbers, Int. J. Heat Mass Transf. 36 (1993) 3437–3448.
[10] C.O. Gersey, I. Mudawar, Effects of heater length and orientation on the trigger mechanism for near-saturated flow boiling CHF–II. CHF model, Int. J. Heat Mass Transf. 38 (1995) 643–654.
[11] G. Liang, I. Mudawar, Review of single-phase and two-phase nanofluid heat transfer in macro-channels and micro-channels, Int. J. Heat Mass Transf. 136 (2019) 324–354.
[12] W. Qu, I. Mudawar, Thermal design methodology for high-heat-flux single-phase and two-phase micro-channel heat sinks, in: Proceedings of the. I-Therm, CA, San Diego, 2002, pp. 347–359. May 29-June 1.
[13] S. Mukherjee, I. Mudawar, Pumpless loop for narrow channel and micro-channel boiling, J. Electron. Packag. 125 (2003) 431–441.
[14] M.E. Johns, I. Mudawar, An ultra-high power two-phase jet-impingement avionic clamshell module, J. Electron. Packag. 118 (1996) 264–270.
[15] G. Liang, I. Mudawar, Review of spray cooling – Part 1: Single-phase and nucleate boiling regimes, and critical heat flux, Int. J. Heat Mass Transf. 115 (2017) 1174–1205.
[16] M.K. Sung, I. Mudawar, Single-phase and two-phase heat transfer characteristics of low temperature hybrid micro-channel/micro-jet impingement cooling module, Int. J. Heat Mass Transf. 51 (2008) 3882–3895.
[17] Z. Liu, R.H.S. Winterton, A general correlation for saturated and subcooled flow boiling in tubes and annuli, based on a nucleate pool boiling equation, Int. J. Heat Mass Transf. 34 (1991) 2759–2766.
[18] L. Sun, K. Mishima, An evaluation of prediction methods for saturated flow boiling heat transfer in mini-channels, Int. J. Heat Mass Transf. 52 (2009) 5323–5329.
[19] W. Zhang, T. Hibiki, K. Mishima, Correlations of two-phase frictional pressure drop and void fraction in mini-channel, Int. J. Heat Mass Transf. 53 (2010) 453–465.
[20] W. Li, Z. Wu, A general criterion for evaporative heat transfer in micro/mini-channels, Int. J. Heat Mass Transf. 53 (2010) 1967–1976.
[21] W. Li, Z. Wu, Generalized adiabatic pressure drop correlations in evaporative micro/mini-channels, Exp. Therm. Fluid Sci. 35 (2011) 866–872.
[22] S.M. Kim, I. Mudawar, Universal approach to predicting two-phase frictional pressure drop for adiabatic and condensing mini/micro-channel flows, Int. J. Heat Mass Transf. 55 (2012) 3246–3261.
[23] S.M. Kim, I. Mudawar, Universal approach to predicting saturated flow boiling heat transfer in mini/micro-channels – Part I. Dryout incipience quality, Int. J. Heat Mass Transf. 64 (2013) 1226–1238.
[24] S.M. Kim, I. Mudawar, Universal approach to predicting saturated flow boiling heat transfer in mini/micro-channels – Part II. Two-phase heat transfer coefficient, Int. J. Heat Mass Transf. 64 (2013) 1239–1256.
[25] J.E. Galloway, I. Mudawar, CHF mechanism in flow boiling from a short heated wall—II. Theoretical CHF model, Int. J. Heat Mass Transf. 36 (1993) 2527–2540.
[26] W.L. Cheng, F.Y. Han, Q.N. Liu, R. Zhao, H. Fan, Experimental and theoretical investigation of surface temperature non-uniformity of spray cooling, Energy 36 (2011) 249–257.
[27] S.M. Kim, I. Mudawar, Theoretical model for annular flow condensation in rectangular micro-channels, Int. J. Heat Mass Transf. 55 (2012) 958–970.
[28] S.M. Kim, I. Mudawar, Theoretical model for local heat transfer coefficient for annular flow boiling in circular mini/micro-channels, Int. J. Heat Mass Transf. 73 (2014) 731–742.
[29] W. Lee, G. Son, H.Y. Yoon, Direct numerical simulation of flow boiling in a finned microchannel, Int. Commun. Heat Mass Transf. 39 (2012) 1460–1466.
[30] S. Osher, J.A. Sethian, Fronts propagating with curvature-dependent speed: Algorithms based on Hamilton-Jacobi formulations, J. Comput. Phys. 79 (1988) 12–49.
[31] C.W. Hirt, B.D. Nichols, Volume of fluid (VOF) method for the dynamics of free boundaries, J. Comput. Phys. 39 (1981) 201–225.
[32] Z. Guo, B.S. Haynes, D.F. Fletcher, Numerical simulation of annular flow boiling in microchannels, J. Comput. Multiph. Flows 8 (2016) 61–82.
[33] Y. Luo, W. Li, K. Zhou, K. Sheng, S. Shao, Z. Zhang, J. Du, W.J. Minkowycz, Three--dimensional numerical simulation of saturated annular flow boiling in a narrow rectangular microchannel, Int. J. Heat Mass Transf. 149 (2020) 119246.
[34] M. Bahreini, A. Ramiar, A.A. Ranjbar, Numerical simulation of bubble behavior in subcooled flow boiling under velocity and temperature gradient, Nucl. Eng. Des. 293 (2015) 238–248.
[35] J. Peng, D. Chen, J. Xu, L. Hu, H. Liu, CFD simulation focusing on void distribution of subcooled flow boiling in circular tube under rolling condition, Int. J. Heat Mass Transf. 156 (2020) 119790.
[36] Z. Yang, X.F. Peng, P. Ye, Numerical and experimental investigation of two phase flow during boiling in a coiled tube, Int. J. Heat Mass Transf. 51 (2008) 1003–1016.
[37] M. Darzi, C. Park, Numerical investigation of horizontal two-phase plug/bubble flows: Gravitational effect on hydrodynamic characteristics, Eur. J. Mech. B Fluids 74 (2019) 342–350.
[38] M. Bahreini, A. Ramiar, A.A. Ranjbar, Numerical simulation of subcooled flow boiling under conjugate heat transfer and microgravity condition in a vertical mini channel, Appl. Therm. Eng. 113 (2017) 170–185.
[39] R. Agarwal, R.S. Dondapati, Numerical investigation on hydrodynamic characteristics of two-phase flow with liquid hydrogen through cryogenic feed lines at terrestrial and microgravity, Appl. Therm. Eng. 173 (2020) 115240.
[40] Y. Zheng, H. Chang, J. Chen, H. Chen, S. Shu, Effect of microgravity on flow boiling heat transfer of liquid hydrogen in transportation pipes, Int. J. Hydrog. Energy 44 (2019) 5543–5550.
[41] J. Lee, L.E. O'Neill, S. Lee, I. Mudawar, Experimental and computational investigation on two-phase flow and heat transfer of highly subcooled flow boiling in vertical upflow, Int. J. Heat Mass Transf. 136 (2019) 1199–1216.
[42] J. Lee, L.E. O'Neill, I. Mudawar, 3-D computational investigation and experimental validation of effect of shear-lift on two-phase flow and heat transfer characteristics of highly subcooled flow boiling in vertical upflow, Int. J. Heat Mass Transf. 150 (2020) 119291.
[43] J. Lee, L.E. O'Neill, I. Mudawar, Computational prediction of key heat transfer mechanisms and hydrodynamic characteristics of critical heat flux (CHF) in subcooled vertical upflow boiling, Int. J. Heat Mass Transf. 161 (2020) 120262.
[44] Y. Sato, K. Sekohuchi, Liquid velocity distribution in two-phase bubble flow, Int. J. Multiphase Flow 2 (1975) 79–95.
[45] Y. Sato, M. Sadatomi, K. Sekoguchi, Momentum and heat transfer in two-phase bubble flow – I. Theory, Int. J. Multiph. Flow 7 (1981) 167–177.
[46] A. Vaidheeswaran, T. Hibiki, Bubble-induced turbulence modeling for vertical bubbly flows, Int. J. Heat and Mass Transf. 115 (2017) 741–752.
[47] M. Lopez de Bertodano, S.J. Lee, R.T. Lahey, D.A. Drew, The Prediction of two-phase turbulence and phase distribution phenomena using a Reynolds stress model, J. Fluids Eng. 112 (1990) 107–113.
[48] M.A. Amidu, Y. Addad, Bubble-induced enhancement of single-phase liquid forced convection heat transfer during subcooled nucleate flow boiling, Ann. Nucl. Energy 134 (2019) 60–66.
[49] Y. Liao, T. Ma, E. Krepper, D. Lucas, J. Fröhlich, Application of a novel model for bubble-induced turbulence to bubbly flows in containers and vertical pipes, Chem. Eng. Sci. 202 (2019) 55–69.
[50] H. Lee, C.R. Kharangate, N. Mascarenhas, I. Park, I. Mudawar, Experimental and computational investigation of vertical downflow condensation, Int. J. Heat Mass Transf. 85 (2015) 865–879.
[51] S.V. Patankar, Numerical heat transfer and fluid flow, Hemisphere Publishing Corp., New York, 1980.

[52] D. Vahl, G.D. Mallinson, False diffusion in numerical fluid dynamics, School of Mechanical and Industrial Engineering, University of New South Wales, 1972 Report 1972/FMT/1.
[53] K.K. So, X.Y. Hu, N.A. Adams, Anti-diffusion method for interface steepening in two-phase incompressible flow, J. Comput. Phys. 230 (2011) 5155–5177.
[54] J. Klostermann, K. Schaake, R. Schwarze, Numerical simulation of a single rising bubble by VOF with surface compression, Int. J. Numer. Meth. Fluids 71 (2013) 960–982.
[55] J.U. Brackbill, D.B. Kothe, C. Zemach, A continuum method for modeling surface tension, J. Comput. Physics 100 (1992) 335–354.
[56] J.F. Klausner, R. Mei, D.M. Bernhard, L.Z. Zeng, Vapor bubble departure in forced convection boiling, Int. J. Heat Mass Transf. 36 (1993) 651–662.
[57] W.H. Lee, A Pressure iteration scheme for two-phase flow modeling, in: T.N. Veziroglu (Ed.), Multi-Phase Transport: Fundamentals, Reactor Safety, Applications, vol. 1, Hemisphere Publishing, Washington, DC, 1980.
[58] C. Kunkelmann, P. Stephan, CFD simulation of boiling flows using the volume-of-fluid method within OpenFOAM, Num. Heat Transf. Part A 56 (2009) 631–646.
[59] ANSYS Fluent user's guide, ANSYS Inc., Canonsburg, PA, 2015.